Check for updates

Received: 16 November 2023 | Revised: 15 February 2024 | Accepted: 28 February 2024

DOI: 10.1002/nbm.5150

RESEARCH ARTICLE

NMR IN BIOMEDICINE WILEY

The Larmor frequency shift of a white matter magnetic microstructure model with multiple sources

Anders Dyhr Sandgaard[1] | Noam Shemesh[2] | Leif Østergaard[1] | Valerij G. Kiselev[3] | Sune Nørhøj Jespersen[1,4]

[1]Center of Functionally Integrative Neuroscience, Department of Clinical Medicine, Aarhus University, Aarhus, Denmark

[2]Champalimaud Research, Champalimaud Centre for the Unknown, Lisbon, Portugal

[3]Division of Medical Physics, Department of Radiology, University Medical Center Freiburg, Freiburg, Germany

[4]Department of Physics and Astronomy, Aarhus University, Aarhus, Denmark

Correspondence
Sune Nørhøj Jespersen, Center of Functionally Integrative Neuroscience, Department of Clinical Medicine, Aarhus University, Aarhus, Denmark.
Email: sune@cfin.au.dk

Funding information
Danmarks Frie Forskningsfond, Grant/Award Numbers: 8020-00158B, 3103-00144B; Lundbeck Foundation, Grant/Award Number: R310-2018-3455

Abstract

Magnetic susceptibility imaging may provide valuable information about chemical composition and microstructural organization of tissue. However, its estimation from the MRI signal phase is particularly difficult as it is sensitive to magnetic tissue properties ranging from the molecular to the macroscopic scale. The MRI Larmor frequency shift measured in white matter (WM) tissue depends on the myelinated axons and other magnetizable sources such as iron-filled ferritin. We have previously derived the Larmor frequency shift arising from a dense medium of cylinders with scalar susceptibility and arbitrary orientation dispersion. Here, we extend our model to include microscopic WM susceptibility anisotropy as well as spherical inclusions with scalar susceptibility to represent subcellular structures, biologically stored iron, and so forth. We validate our analytical results with computer simulations and investigate the feasibility of estimating susceptibility using simple iterative linear least squares without regularization or preconditioning. This is done in a digital brain phantom synthesized from diffusion MRI measurements of an ex vivo mouse brain at ultra-high field.

KEYWORDS
Larmor frequency, Lorentz cavity, magnetic microstructure, magnetic susceptibility, modelling, quantitative susceptibility mapping

1 | INTRODUCTION

The Larmor frequency of an MR-visible fluid in tissue is perturbed by microscopic variations in magnetic field induced by the sample. This microscopically varying magnetic field is determined by the tissue's magnetic susceptibility. In biological tissues, such microscopic perturbations are affected by the cellular and even subcellular tissue composition and configuration. Given the likely relevance of these tissue scales to early stages of disease,[1–4] where subtle micro-architectural modulations may occur, it is highly desirable to accurately measure the magnetic tissue properties that drive the frequency perturbations. However, as the nominal MRI resolution on clinical scanners (typically millimeters) is orders of magnitude greater than the microstructure (typically micrometers), such microscopic Larmor frequency perturbations become coarse grained (fine details are

Abbreviations: dMRI, diffusion MRI; DNR, diffusion-narrowing regime (homogenous broadened spectral lineshape); FA, fractional anisotropy; fODF, fiber orientation distribution function; GLTA, generalized Lorentzian tensor approach; GM, gray matter; MBP, myelin basic protein; MD, mean diffusivity; MW, myelin water; PLP, proteolipid protein; QSM, quantitative susceptibility mapping; RMSE, root-mean-squared error; SNR, signal-to-noise ratio; STI, susceptibility tensor imaging; WM, white matter.

This is an open access article under the terms of the Creative Commons Attribution-NonCommercial-NoDerivs License, which permits use and distribution in any medium, provided the original work is properly cited, the use is non-commercial and no modifications or adaptations are made.
© 2024 The Authors. *NMR in Biomedicine* published by John Wiley & Sons Ltd.

smoothed) on the mesoscopic scale (typically 10–100 μm) both by the measurement itself and by diffusion.[5] Nonetheless, a signature of the mesoscopically averaged magnetized microstructure remains embedded in the measured Larmor frequency shift.[6–9]

Understanding how magnetic susceptibility of tissue gives rise to a measurable Larmor frequency shift has been an active field of research for decades.[10–20] In addition, efforts have focused on inverting this relationship to estimate local magnetic susceptibility in the brain, resulting in the common methods dubbed quantitative susceptibility mapping (QSM)[21] and susceptibility tensor imaging (STI)[22]. Unfortunately, these inversion methods do not account for microscopic variations in the Larmor frequency shifts from susceptibility sources at microscopic distances from the reporting MR fluid. Failing to account for such microscopic features can ultimately lead to a substantial bias in susceptibility estimation[23]—especially in white matter (WM).

Incorporating such microscopic variations in the Larmor frequency shift into current QSM/STI models[24] requires explicit attention to the *microscopic magnetic anisotropy* of tissue in the sample. This includes *microscopic susceptibility anisotropy* (e.g., of the alkyl chain of the myelin sheath[25]) and *microscopic structural anisotropy* (e.g., from the cylindrical geometry of WM axons, as can be seen in Figure 2 later). Both types of anisotropy give rise to an anisotropic Larmor frequency shift[8,25,30–34] that depends on the angle between the main magnetic field and directions of the axons. This has led to the development of several analytical models,[11,13,14,24,34-36] (e.g., describing the local microscopic Larmor frequency shift caused by microscopic magnetic anisotropy of WM). In particular, Wharton and Bowtell[13] and Sukstanskii and Yablonskiy[14] solved the magnetostatic equations to describe the microscopic Larmor frequency shift from a single infinitely long hollow cylinder accounting for both types of microscopic magnetic anisotropy of the myelin sheath. Sukstanskii and Yablonskiy[14] also considered each surrounding fluid compartment to have a scalar magnetic susceptibility different from the NMR fluid (e.g., to model iron-containing cells).

Due to the resolution of MRI measurement and the inherent diffusion of the MR-visible fluid, microscopic variations in the Larmor frequency must be coarse-grained on the mesoscopic scale in descriptions of the measured Larmor frequency shift. To account for this averaging, He and Yablonskiy[34] and later Yablonskiy and Sukstanskii[11] proposed a general framework dubbed the generalized Lorentzian approach (GLA) and generalized Lorentzian tensor approach (GLTA), respectively. As illustrated in Figure 1, the approach followed the original concept of Lorentz[37,38]: Here, the main idea is to divide the whole sample (Figure 1A) into two regions around the point of interest: a *near* region (Figure 1B) and a *far* region (Figure 1C). The size of the near region should be larger than the characteristic size of the microstructure such that the frequency shift induced from sources in the far region can be described by a locally averaged magnetic susceptibility and the overall sample shape. This is the reason for calling the size of the near region *mesoscopic*,[7,20,37,38] in comparison with the conventional molecular sized Lorentz cavity[7,12,20,37-40] used in the context of NMR to describe the frequency shift in isotropic liquids. The far region comprises the whole sample excluding a mesoscopic Lorentz cavity (the near region) around the point at which this coarse-grained Larmor frequency shift is considered. The frequency shift induced from sources within the near region must be calculated with account for the explicit magnetized microstructure and diffusion of the MR-visible fluid, as distances here are comparable with the characteristic length of the microstructure. Since the shape of this mesoscopic cavity can be chosen at our convenience,[9] the main idea in the GL(T)A model is to identify a shape of the cavity (a so-called Lorentzian boundary) such that the mean frequency shift, which originates from the contained magnetized microstructure within it, can be neglected. By analogy, introducing a spherical molecular Lorentz cavity for isotropic liquids allows one to neglect an explicit calculation at the molecular scale[7,39] in isotropic liquids. On the mesoscopic scale, the shape of the cavity is less trivial as it relates to the total *magnetic anisotropy* of the microstructure. If the susceptibility is constant over the magnetized objects, the shape of the Lorentz cavity relates only to the *structural anisotropy* of the microstructure. If the microstructure is simple and its susceptibility constant, for example, contains either uniformly magnetized parallel cylinders or spheres, the boundary is a coaxial cylinder or sphere, respectively. Hence, when this Lorentzian boundary of the mesoscopic cavity can be identified, such that an explicit calculation of the frequency shift inside the mesoscopic cavity can be avoided, only the averaged sources in the far region (Figure 1C) need to be considered, and one only has to account for the correction due to the shape of the subtracted mesoscopic cavity. In the GLTA model,[11] this mesoscopic correction was defined by a so-called Lorentzian tensor, which contains information about the average susceptibility and microstructure inside the mesoscopic cavity (Figure 1B). As a model of WM microstructure, explicit expressions for the Lorentzian tensor were presented in the GLTA model for both solid parallel cylinders and spheres, assuming a low volume fraction and uniform susceptibility.

Explicit calculation of this Lorentzian tensor is generally difficult—especially for dense media including multiple types of inclusion—and identifying the appropriate shape of the mesoscopic cavity quickly becomes non-trivial. To overcome this, Ruh et al. and Kiselev[6,36] derived the dependence of the Lorentzian tensor for an arbitrary microstructure on its structural correlation function—as long as the susceptibility (scalar or tensor) remains uniform over the magnetized objects. The important difference here, compared with the GL(T)A model, is thinking of the microstructure in terms of the correlation function instead of the shape of the mesoscopic cavity. Ruh et al. and Kiselev[6,36] also reproduced the results for randomly positioned parallel solid cylinders with arbitrary volume fraction, and later Sandgaard et al.[9,24] extended the result to uniformly magnetized multi-layered cylinders with arbitrary orientations using the correlation function approach.

Current models of the Lorentzian tensor fail to capture salient WM features as they assume that WM axons occupy a low volume fraction, that WM axons are parallel, that microscopic magnetic susceptibility is uniform, and so on. In reality, axon orientations are dispersed (at least by 20–30°; Reference 41), occupy a large fraction of the WM volume (around 30%), and possess non-uniform magnetic susceptibility.[25,33] Furthermore, experiments have demonstrated that biologically stored iron in WM, such as ferritin, affects the Larmor frequency shift.[42–46] All such realistic features should ideally be addressed in a model of the Larmor frequency shift in WM.

10991492, 2024, 8, Downloaded from https://analyticalsciencejournals.onlinelibrary.wiley.com/doi/10.1002/nbm.5150 by Cochrane Portugal, Wiley Online Library on [09/01/2025]. See the Terms and Conditions (https://onlinelibrary.wiley.com/terms-and-conditions) on Wiley Online Library for rules of use; OA articles are governed by the applicable Creative Commons License

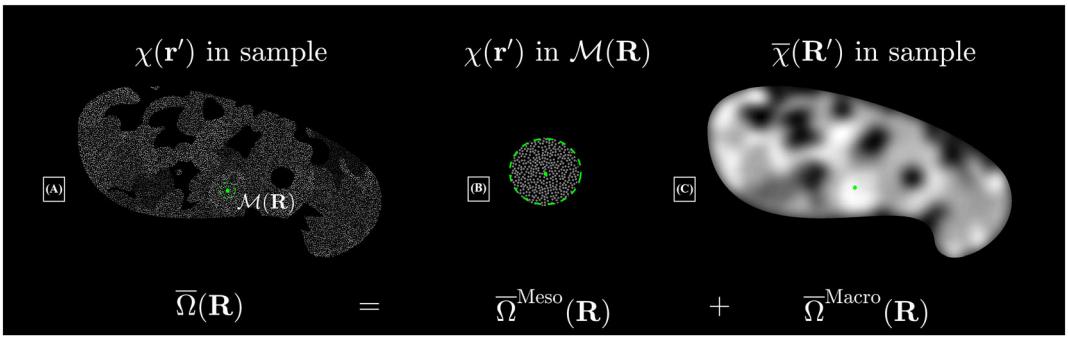

FIGURE 1 Magnetic microstructure model: local magnetic susceptibility $\chi(\boldsymbol{r}')$ from multiple regions with an associated microstructure. **A**, The coarse-grained Larmor frequency $\overline{\Omega}(\mathbf{R})$ is given by the microscopic Larmor frequency $\Omega(\boldsymbol{r})$ felt by a spin at position $\boldsymbol{r}$ averaged within a mesoscopic sphere $\mathcal{M}(\mathbf{R})$. **B**, **C**, $\overline{\Omega}(\mathbf{R})$ can be described by two contributions. **B**, The first is the contribution from explicit microstructure within $\mathcal{M}(\mathbf{R})$, which defines the mesoscopic Larmor frequency $\overline{\Omega}^{\mathrm{Meso}}(\mathbf{R})$. **C**, The second contribution depends on the Larmor frequency at **R** induced by the mesoscopic averaged magnetic microstructure $\overline{\chi}(\mathbf{R}')$. This defines the local macroscopic Larmor frequency $\overline{\Omega}^{\mathrm{Macro}}(\mathbf{R})$. The image illustrates a mesoscopic spherical cavity in $\overline{\Omega}^{\mathrm{Macro}}(\mathbf{R})$.

In this study, we derive the Lorentzian tensor for non-uniform microscopic magnetic susceptibility and present new analytical results for the mesoscopically averaged (coarse-grained) Larmor frequency shift. Our biophysical model of WM consists of a dense medium of orientationally dispersed, multi-layered cylinders with microscopic susceptibility anisotropy to model axons, and spherical inclusions in all major water compartments to model subcellular structures, biologically stored iron, and so on. We describe how this complicated microstructure gives rise to a set of effective susceptibility parameters from all the susceptibility sources, and six structural parameters that describe the axonal orientation dispersion, which can be determined independently from diffusion MRI (dMRI).

2 | THEORY

In this section, we first outline the system of consideration. We then revisit the theoretical framework for the mesoscopically averaged Larmor frequency shift $\overline{\Omega}(\mathbf{R})$. Third, we present analytical results for a biophysical model of WM magnetic microstructure incorporating both orientationally dispersed WM axons with microscopic susceptibility anisotropy and spherical inclusions representing, for example, biologically stored iron. Last, our main analytical result for the model-specific mesoscopic Larmor frequency shift $\overline{\Omega}(\mathbf{R})$ is presented, while a complete derivation can be found in Supporting information.

2.1 | System of consideration

The macroscopic sample of volume V is described as a porous medium of impermeable microscopic magnetizable inclusions immersed in an MR-visible fluid. The inclusions are magnetized by the external field $\mathbf{B}_0 = B_0\hat{\mathbf{B}}$, where $\hat{\mathbf{B}}$ is a unit vector. All inclusions are assumed to be weakly dia- or paramagnetic, and characterized for each inclusion by a magnetic susceptibility tensor $\boldsymbol{\chi}^{\mathrm{Q}}(\boldsymbol{r})$ ($|\chi| \ll 1$, and is given relative to the susceptibility of the MR fluid with susceptibility χ^{W} and volume fraction ζ^{W}).

2.2 | Mesoscopic Larmor frequency shift $\overline{\Omega}(\mathbf{R})$

The Larmor frequency $\overline{\Omega}(\mathbf{R})$ describes the average microscopic frequency shifts felt by the MR-visible fluid inside a mesoscopic region $\mathcal{M}$ at position **R** (cf. Figure 1). When $\overline{\Omega}(\mathbf{R})$ does not vary across the sampling point spread function, it provides an approximation to the MRI-measured Larmor frequency shift, i.e., $\overline{\Omega}_{\mathrm{MRI}}(\mathbf{R}) = \overline{\Omega}(\mathbf{R})$ inside a voxel at position **R**.[9,24,36] This mesoscopic Larmor frequency shift can be described by a mesoscopic contribution $\overline{\Omega}^{\mathrm{Meso}}(\mathbf{R})$, which is the mean induced frequency shift in $\mathcal{M}$ from the actual distribution of sources within $\mathcal{M}$, a macroscopic contribution $\overline{\Omega}^{\mathrm{Macro}}(\mathbf{R})$ describing the mean induced Larmor frequency shift in $\mathcal{M}$ from distant sources outside $\mathcal{M}$, and an additional contribution $\overline{\Omega}^{\mathrm{W}}(\mathbf{R})$ describing the mean induced Larmor frequency shift in $\mathcal{M}$ from the whole sample with susceptibility χ^{W}:

$$\overline{\Omega}(\mathbf{R}) = \overline{\Omega}^{\mathrm{Meso}}(\mathbf{R}) + \overline{\Omega}^{\mathrm{Macro}}(\mathbf{R}) + \overline{\Omega}^{\mathrm{W}}(\mathbf{R}). \tag{1}$$

10991492, 2024, 8, Downloaded from https://analyticalsciencejournals.onlinelibrary.wiley.com/doi/10.1002/nbm.5150 by Cochrane Portugal, Wiley Online Library on [09/01/2025]. See the Terms and Conditions (https://onlinelibrary.wiley.com/terms-and-conditions) on Wiley Online Library for rules of use; OA articles are governed by the applicable Creative Commons License

This decomposition is visualized in Figure 1. In general, the shape of $\mathcal{M}$ can always be chosen for our convenience. Here we choose $\mathcal{M}$ to be spherical, as it represents the best compromise when working with a general magnetic microstructure. While the shape of $\mathcal{M}$ may affect the values of $\overline{\Omega}^{\text{Meso}}(\mathbf{R})$ and $\overline{\Omega}^{\text{Meso}}(\mathbf{R})$ individually, the sum $\overline{\Omega}^{\text{Meso}}(\mathbf{R})+\overline{\Omega}^{\text{Macro}}(\mathbf{R})$ remains unchanged. Each contribution will be described in turn.

2.2.1 | Mesoscopic contribution $\overline{\Omega}^{\text{Meso}}(\mathbf{R})$

The microscopic Larmor frequency shift sensed by the MR fluid depends in general on time due to water diffusion. This in turn means that the mesoscopic contribution $\overline{\Omega}^{\text{Meso}}(\mathbf{R})$ to $\overline{\Omega}(\mathbf{R})$ may depend on time. However, as described in a previous study[9]: considering long times in comparison to the diffusion time $\tau_c = {l_c}^2/D$ of the microstructure, where l_c is the characteristic length of the microstructure and D the diffusivity, the mesoscopic contribution becomes time independent. This regime is the so-called diffusion-narrowing regime (DNR).[47] Here $\overline{\Omega}^{\text{Meso}}(\mathbf{R})$ is described by a Lorentzian tensor $\mathbf{L}$ of the magnetic microstructure inside a mesoscopic sphere $\mathcal{M}$[6,7,34,37,38] surrounding $\mathbf{R}$ (see previous work[9] on the freedom of choosing the shape of $\mathcal{M}$)

$$\overline{\Omega}^{\text{Meso}}(\mathbf{R}) = \gamma B_0 \widehat{\mathbf{B}}^{\mathsf{T}} \mathbf{L} \widehat{\mathbf{B}}, \tag{2}$$

where

$$\mathbf{L} = \frac{1}{\zeta^{\text{W}}} \int \frac{d\boldsymbol{k}}{(2\pi)^3} \boldsymbol{\Upsilon}(\boldsymbol{k}) \boldsymbol{\Gamma}(\boldsymbol{k}). \tag{3}$$

Here $\boldsymbol{\Upsilon}(\boldsymbol{k})$ is the elementary dipole kernel in Fourier space including a molecular Lorentz correction[39] and ζ^{W} the total water volume fraction outside all inclusion types. Equation (3) depends in turn on the tensor-valued magneto-structural cross-correlation function[9] $\boldsymbol{\Gamma}(\boldsymbol{k})$,

$$\boldsymbol{\Gamma}(\boldsymbol{k}) = \frac{v^{\text{W}}(\boldsymbol{k}) \chi(-\boldsymbol{k})}{|\mathcal{M}|}, k > 0, \tag{4}$$

and zero for $k = 0$. For notational simplicity, we leave it understood implicitly that the cross-correlations in Equations (2)–(4) are considered in the vicinity of $\mathbf{R}$. The size $|\mathcal{M}|$ denotes the volume of the mesoscopic sphere needed[9] to average the magnetic microstructure near $\mathbf{R}$, and to allow the exterior to be described by an averaged (bulk) magnetic microstructure[9] $\overline{\chi}(\mathbf{R})$. Here $v^{\text{W}}(\boldsymbol{k})$ is the total indicator function of the reporting water surrounding the microscopic inclusions while $\chi(\boldsymbol{k})$ denotes the microscopic susceptibility tensor of the inclusions in k-space. Our definition of the Lorentzian tensor $\mathbf{L}$ differs from the GLTA model: here an isotropic medium gives $\mathbf{L} = \mathbf{0}$, while the GLTA model predicts $\mathbf{L}_{\text{GLTA}} = \mathbf{I}/3$. This does not mean that the two models disagree, as it is merely a rearrangement of terms in $\overline{\Omega}^{\text{Meso}}(\mathbf{R})+\overline{\Omega}^{\text{Macro}}(\mathbf{R})$ such that the sum remains unchanged.

If the magnetic susceptibility is constant inside the inclusions (scalar or tensor), $\mathbf{L} = -\mathbf{N}\chi$ is described by a demagnetization tensor $\mathbf{N}$

$$\mathbf{N} = -\frac{1}{\zeta^{\text{W}}} \int \frac{d\boldsymbol{k}}{(2\pi)^3} \boldsymbol{\Upsilon}(\boldsymbol{k}) \Gamma(\boldsymbol{k}), \tag{5}$$

which depends only on the structure–structure correlation function

$$\Gamma(\boldsymbol{k}) = \frac{v^{\text{W}}(\boldsymbol{k}) v(-\boldsymbol{k})}{|\mathcal{M}|}, k > 0. \tag{6}$$

In general, the MR fluid is weighted by differences in transverse relaxation, but if all the fluid contributes equally to the frequency shift in $\mathcal{M}$, the fluid indicator function $v^{\text{W}}(\boldsymbol{r}) = 1 - v(\boldsymbol{r})$ relates to the structural indicator function $v(\boldsymbol{r})$ of all inclusions. By choosing $\mathcal{M}$ as a sphere, there is no need to consider the 1 in v^{W} in Equation (4) since it does not contribute when substituted in Equation (3) (corresponding to the Lorentz-corrected field inside a homogenously magnetized sphere[39]). This means that the mean magnetic field in $v^{\text{W}}(\boldsymbol{r})$ is equal and opposite in sign to the field inside $v(\boldsymbol{r})$. The correlation tensor $\boldsymbol{\Gamma}(\boldsymbol{k})$ extends the previous description of $\mathbf{L}(\mathbf{R})$ to include non-uniform susceptibility, while previous work described uniformly magnetized inclusions reducing $\boldsymbol{\Gamma}(\boldsymbol{k})$ to the structural correlation function $\Gamma(\boldsymbol{k})$.

10991492, 2024, 8, Downloaded from https://analyticalsciencejournals.onlinelibrary.wiley.com/doi/10.1002/nbm.5150 by Cochrane Portugal, Wiley Online Library on [09/01/2025]. See the Terms and Conditions (https://onlinelibrary.wiley.com/terms-and-conditions) on Wiley Online Library for rules of use; OA articles are governed by the applicable Creative Commons License

2.2.2 | Macroscopic contribution $\overline{\Omega}^{\text{Macro}}(\mathbf{R})$

The mesoscopically averaged Larmor frequency shift $\overline{\Omega}^{\text{Macro}}(\mathbf{R})$ inside $\mathcal{M}$ caused by sources outside of $\mathcal{M}$ does not depend on explicit microscopic details of $v(\boldsymbol{r})$ and $\chi(\boldsymbol{r})$—only averaged properties[9] such as the bulk magnetic susceptibility $\overline{\chi}(\mathbf{R})$ matter:

$$\overline{\Omega}^{\text{Macro}}(\mathbf{R}) = \gamma B_0 \widehat{\mathbf{B}}^{\mathsf{T}} \int \Upsilon(\mathbf{R}-\mathbf{R}')\overline{\chi}(\mathbf{R}')\widehat{\mathbf{B}}, \quad (\mathcal{M} \text{ is spherical}). \tag{7}$$

Since $\mathcal{M}$ was chosen as a sphere, integration can be performed over the whole sample volume, as integrating $\overline{\chi}(\mathbf{R})$ inside $\mathcal{M}$ yields zero due to the Lorentz-sphere correction in Υ. If the shape of $\mathcal{M}$ is different (e.g., a cylinder), integration over $\mathcal{M}$ must be subtracted in Equation (7). Subtracting a cylindrical cavity in $\overline{\Omega}^{\text{Macro}}(\mathbf{R})$ should therefore not be forgotten when including the mean microscopic field described by previous single hollow cylinder models.[13] In MRI, the Larmor frequency shift is sampled at discrete positions $\mathbf{R}'$. In this case, the macroscopic contribution $\overline{\Omega}^{\text{Macro}}(\mathbf{R})$ can be approximated on the level of the sampling resolution by a discrete convolution between a voxel-averaged dipole field[9] $\overline{\Upsilon}(\mathbf{R})$ and the averaged magnetic susceptibility $\overline{\chi}(\mathbf{R})$ across the sample

$$\overline{\Omega}^{\text{Macro}}(\mathbf{R}) \approx \gamma B_0 \widehat{\mathbf{B}}^{\mathsf{T}} \sum_{\mathbf{R}'} \overline{\Upsilon}(\mathbf{R}-\mathbf{R}')\overline{\chi}(\mathbf{R}')\widehat{\mathbf{B}}. \tag{8}$$

Here the whole sample has been partitioned into voxels at discrete positions $\mathbf{R}$ with size described by the sampling resolution. The sample shape is thus represented implicitly by the sum. Notice that Equation (8) corresponds to the frequency shift considered in STI and QSM, although they typically use the elementary dipole field $\Upsilon(\mathbf{R})$ and not the voxel-averaged $\overline{\Upsilon}(\mathbf{R})$, which can lead to a bias in parameter estimation.[9]

2.2.3 | Frequency shift $\overline{\Omega}^{\text{W}}(\mathbf{R})$ from MR fluid

The last frequency shift from the MR fluid depends on its susceptibility χ^{W} and the sample shape

$$\overline{\Omega}^{W}(\mathbf{R}) = \chi^{W} \gamma B_0 \widehat{\mathbf{B}}^{\mathsf{T}} \mathbf{N}^{W}(\mathbf{R}) \widehat{\mathbf{B}}. \tag{9}$$

Here $\mathbf{N}^{W}(\mathbf{R})$ defines the sample-specific Lorentz-corrected point-demagnetization tensor[48,49]

$$\mathbf{N}^{W}(\mathbf{R}) = \int d\mathbf{R}' \, \Upsilon(\mathbf{R}-\mathbf{R}'), \tag{10}$$

where the integration is performed over the sample.

2.3 | A WM magnetic microstructure model

To develop robust biophysical models of WM magnetic microstructure that describes the MRI measured Larmor frequency shift, it is important to identify the main features affecting the microscopic Larmor frequency sensed by water molecules. As described previously,[24] there are two main types of microscopic magnetic anisotropy affecting the microscopic Larmor frequency shift: microscopic structural anisotropy and microscopic susceptibility anisotropy. This means that a model should embrace not only microstructural features of tissue, but also susceptibility features due to chemical composition.

In WM, most axons in the central nervous system are insulated by a myelin sheath spiraling around the axon.[50] Figure 2 gives an overview of the construction. The myelin sheath consists of alternating layers of protein-rich water and lipids. Each lipid sheath is constructed mainly from phospholipids, glycolipids, and cholesterol. Their hydrophobic tails combine to form a lipid bilayer such that their hydrophilic heads are in direct contact with the water-filled protein layers, hampering the mobility of water molecules near the interface of the bilayers.[51] The inner protein layers contain amphipathic myelin basic proteins (MBPs) which stabilize the membrane by interacting with the charged heads of the lipids. The outer protein layers are connected to the neighboring membranes via proteolipid protein (PLP) chains and are openly connected to the extracellular space. PLPs form channels for transporting ions or small molecules across the membrane. The water-filled protein layers are extremely thin (around 2–4 nm thick, which is approximately 10 times the size of a water molecule—around 0.3 nm). These protein-rich water compartments are

10991492, 2024, 8, Downloaded from https://analyticalsciencejournals.onlinelibrary.wiley.com/doi/10.1002/nbm.5150 by Cochrane Portugal, Wiley Online Library on [09/01/2025]. See the Terms and Conditions (https://onlinelibrary.wiley.com/terms-and-conditions) on Wiley Online Library for rules of use; OA articles are governed by the applicable Creative Commons License

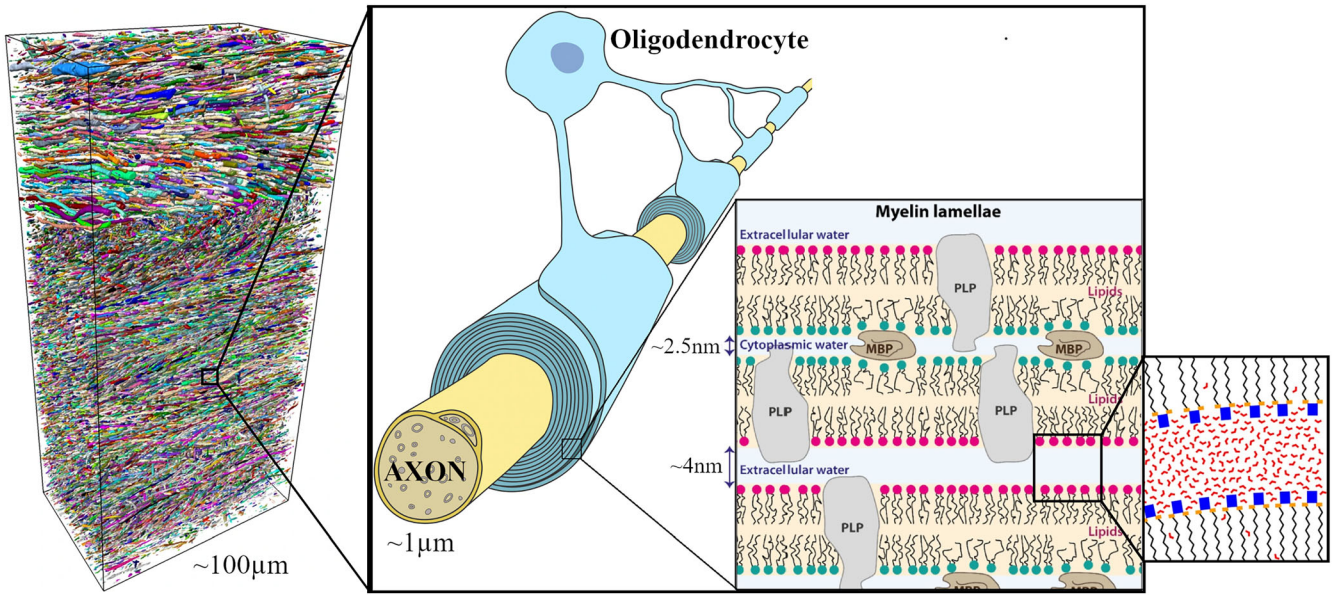

FIGURE 2 Depiction of the myelinated axons in WM. Left: 3D segmentation of myelinated axons in corpus callosum and cingulum of a rat.[26] Right: a myelin sheath is wrapped around the axons, produced by a neighboring oligodendrocyte. The myelin lamellae are comprised of alternating layers of lipid bilayers (yellow background) and protein-rich water layers (blue background). The hydrophobic tails of the lipids attract to form the lipid bilayer, leaving the hydrophilic heads (green and red circles) in direct connection with the water-filled protein layers (cytoplasmic and extracellular water). The MBPs stabilize the lamellae, while the PLPs form channels to allow transportation of ions or small molecules to pass through. As shown on the right, water molecules in protein-rich MW form a hydration later near the hydrophilic heads of the lipids. The illustration is adapted and reprinted from References 26–28 with permission from Elsevier, Creative Commons and Wiley materials (Copyright © 2013 Wiley Periodicals, Inc.), respectively. The image contains illustrations from Reference 29 with permission from PNAS (exempt from Creative Commons license).

collectively denoted as myelin water (MW). The myelin membranes are produced by externally placed oligodendrocytes interposed between different myelinated axons and can be responsible for myelination of up to 40 myelin segments of different adjoining axons. An important component in myelin production is iron, and oligodendrocytes are the most predominant iron-containing cell in WM.[52] Transferrin is responsible for transporting iron atoms to the oligodendrocytes.[52] If not immediately used in myelin production, the iron atoms are stored in ferritin complexes. A full ferritin complex can store up to 4500 iron atoms.[53] The highest WM iron concentrations are found by iron staining to be in the superficial WM, while deep WM, such as the corpus callosum and optic radiation, is devoid of staining.[54]

The main goal of this study is to generalize existing models[11,13,14,36,40,55] of the Larmor frequency shift in WM described in the introduction. Our model of WM magnetic microstructure embraces the microscopic susceptibility sources with the greatest contributions, including their structural anisotropy, expected to affect the measured Larmor frequency shift the most. Our new magnetic microstructure model of WM (as seen in Figure 3) consists of the following two main groups of sources assumed to be impermeable for water molecules.

Infinitely long cylinders randomly positioned with an arbitrary size distribution independent of their orientations. Each cylinder consists of multiple concentric layers to model the bilayers consisting of lipids, PLP channels, and so one. Each layer has an axially symmetric microscopic susceptibility tensor $\boldsymbol{\chi}^{C}$, which models the radially positioned lipid bilayers[34] such that the magnetic response is $\chi_{\parallel}$ parallel to each lipid and $\chi_{\perp}$ perpendicular.[25] Their positions are described by a microscopic indicator function $v^{C}(\boldsymbol{r})$ (which is 1 inside inclusions and 0 otherwise), and their total volume fraction by ζ^{C}. This extends our previous proposed model for solid and multilayered cylinders with arbitrary orientation dispersion,[9] and goes beyond previous descriptions of WM magnetic tissue heterogeneity. The magnetic susceptibility $\boldsymbol{\chi}^{C}$ of each layer-forming lipid inclusion of the axons pointing along the radial direction $\hat{\boldsymbol{u}}$ with respect to the cylinder becomes (cf. Figure 3A)

$$\boldsymbol{\chi}^{C} = \chi_{\perp}\left(\mathbf{I} - \hat{\boldsymbol{u}}\hat{\boldsymbol{u}}^{\mathsf{T}}\right) + \chi_{\parallel}\hat{\boldsymbol{u}}\hat{\boldsymbol{u}}^{\mathsf{T}} = \left(\chi^{C} - \frac{1}{3}\Delta\chi\right)\mathbf{I} + \Delta\chi\hat{\boldsymbol{u}}\hat{\boldsymbol{u}}^{\mathsf{T}}\ (\text{myelin lipid}). \tag{11}$$

Here

$$\chi^{C} = \frac{\chi^{\parallel} + 2\chi^{\perp}}{3} = \frac{1}{3}\mathrm{Tr}(\chi), \text{and } \Delta\chi = \chi_{\parallel} - \chi_{\perp} \tag{12}$$

10991492, 2024, 8, Downloaded from https://analyticalsciencejournals.onlinelibrary.wiley.com/doi/10.1002/nbm.5150 by Cochrane Portugal, Wiley Online Library on [09/01/2025]. See the Terms and Conditions (https://onlinelibrary.wiley.com/terms-and-conditions) on Wiley Online Library for rules of use; OA articles are governed by the applicable Creative Commons License

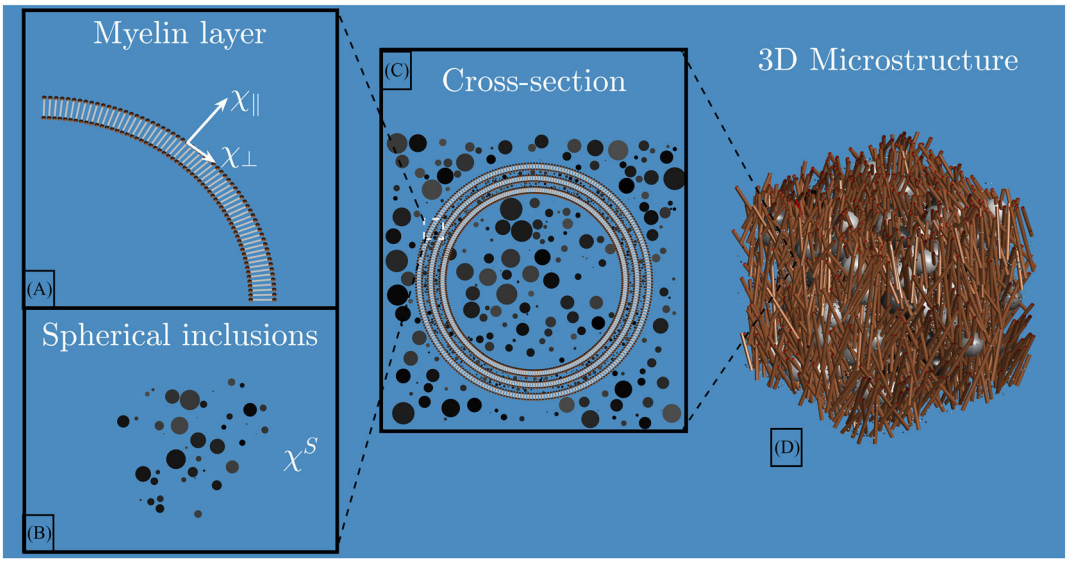

FIGURE 3 Magnetic microstructure model from different perspectives. **A**, The myelin shell assumed to consist of lipid chains and PLPs. The chains exhibit microscopic susceptibility anisotropy $\Delta\chi = \chi_{\parallel} - \chi_{\perp}$. **B**, The different spherical inclusions that can be found in all water layers and can have different sizes and susceptibilities (here shown by varying color and size). **C**, The magnetic microstructure of a single axon with susceptibility sources shown in **A** and **B**. Spherical inclusions with isotropic susceptibility χ^E are randomly positioned outside cylinders and could mimic iron complexes outside axons. Within the bi-layers, MBPs (large spheres) or point-like particles are shown. They possess an isotropic susceptibility χ^M. Intra-axonal point-like spheres with isotropic susceptibility χ^A are also included. The total susceptibility is $\chi^S = \chi^A + \chi^M + \chi^E$ and they are assumed to occupy a low volume fraction in WM. **D**, The entire 3D magnetic microstructure to demonstrate orientation dispersion and other spherical inclusions (e.g., neuroglia). All the proportions are exaggerated for illustrative purposes.

defines one-third of the trace of χ^C and the microscopic susceptibility anisotropy, respectively.

Spherical inclusions randomly positioned in all major water compartments (cf. Figure 3B). Each water compartment contains its own population of spherical inclusions. Each population may reflect multiple spherical sources with different susceptibilities. Here we focus on a single population of spheres in each water compartment for simplicity, but this can naturally be extended to multiple different sources. Hence, each compartmental susceptibility represent a weighted average across all susceptibility sources residing in a given compartment. Spherical inclusions (such as biologically stored iron, e.g., iron-filled ferritin molecules) are assumed to reside in the extra-axonal space with magnetic susceptibility denoted χ^E with volume fraction ζ^E. The distribution of extra-axonal spheres is described by the indicator function $v^E(\boldsymbol{r})$. The distribution of spherical inclusions in the intra-axonal space is described by $v^A(\boldsymbol{r})$ with magnetic susceptibility χ^A and volume fraction ζ^A. The MW layers are assumed to include spherical inclusions such as diamagnetic MBP and other potential sources, and here the susceptibility is denoted χ^M, the volume fraction ζ^M and the indicator function $v^M(\boldsymbol{r})$. All the different spherical inclusions in the water compartments have a total indicator function given by the sum $v^S(\boldsymbol{r}) = v^A(\boldsymbol{r}) + v^M(\boldsymbol{r}) + v^E(\boldsymbol{r})$ and susceptibility $\chi^S(\boldsymbol{r}) = \chi^A v^A(\boldsymbol{r}) + \chi^M v^M(\boldsymbol{r}) + \chi^E v^E(\boldsymbol{r})$. In our model, spheres can have an arbitrary volume fraction, but in practice they are assumed to occupy a low volume fraction in WM, that is, $\zeta^S = \zeta^A + \zeta^M + \zeta^E \ll 1$, which is justified by histological findings.[56]

2.3.1 | Water volume fraction ζ^W and indicator function v^W

The total volume fraction of all inclusions is $\zeta = \zeta^C + \zeta^M + \zeta^E + \zeta^A$. The indicator function $v^W(\boldsymbol{r})$ of the reporting water, Equation (3), is in general weighted by the signal attenuation caused by transverse relaxation, which sets it apart from the purely geometrical indicator functions of the inclusions. If all the water contributes evenly, the water indicator function becomes $v^W(\boldsymbol{r}) = 1 - v^C(\boldsymbol{r}) - v^S(\boldsymbol{r})$, with $\zeta^W = 1 - \zeta$ describing the total water fraction. If MW is fully relaxed, the water indicator function becomes $v^W(\boldsymbol{r}) = 1 - v^C(\boldsymbol{r}) - v^S(\boldsymbol{r}) - v^{MW}(\boldsymbol{r})$ with water volume fraction $\zeta^W = 1 - \zeta^C - \zeta^S - \zeta^{MW}$, where ζ^{MW} denotes the total water volume fraction of the MW compartment. We assume water to be moving around freely in all water compartments. While the assumption of freely moving water may be violated in MW,[28,57,58] the main focus of this study is to consider the case when MW is fully relaxed, as is the case in DNR[47] due to the rapid signal decay of MW.[59,60]

10991492, 2024, 8, Downloaded from https://analyticalsciencejournals.onlinelibrary.wiley.com/doi/10.1002/nbm.5150 by Cochrane Portugal, Wiley Online Library on [09/01/2025]. See the Terms and Conditions (https://onlinelibrary.wiley.com/terms-and-conditions) on Wiley Online Library for rules of use; OA articles are governed by the applicable Creative Commons License

2.4 | Lorentzian tensor of WM magnetic microstructure model

Since two different susceptibility sources $\boldsymbol{\chi}^{\mathrm{C}}$ and χ^{S} are considered here, it is convenient to separate the full Lorentzian tensor $\mathbf{L}$ from both sources into two contributions, cf. Equation (3), since $\mathbf{L}$ is linear with respect to susceptibility. This means that $\mathbf{L}$ can be described by two Lorentzian tensors $\mathbf{L}^{\mathrm{C}}$ and $\mathbf{L}^{\mathrm{S}}$, where $\mathbf{L}^{\mathrm{C}}$ corresponds to the mesoscopic contribution induced by $\boldsymbol{\chi}^{\mathrm{C}}$ and $\mathbf{L}^{\mathrm{S}}$ the mesoscopic contribution induced by the spherical susceptibility χ^{S}:

$$\mathbf{L}=\mathbf{L}^{\mathrm{C}}+\mathbf{L}^{\mathrm{S}}. \tag{13}$$

Here the Lorentzian tensor $\mathbf{L}^{\mathrm{C}}$ is

$$\mathbf{L}^{\mathrm{C}}=-\frac{1}{\zeta^{\mathrm{W}}}\int\frac{d\boldsymbol{k}}{(2\pi)^3}\boldsymbol{\Upsilon}(\boldsymbol{k})\left(v^{\mathrm{MW}}(\boldsymbol{k})+v^{\mathrm{S}}(\boldsymbol{k})+v^{\mathrm{C}}(\boldsymbol{k})\right)\boldsymbol{\chi}^{\mathrm{C}}(-\boldsymbol{k}),\quad(\text{cylinders are sources}). \tag{14}$$

The Lorentzian tensor $\mathbf{L}^{\mathrm{C}}$ describes the measured Larmor frequency shift inside $\mathcal{M}$ from the cylinders with non-uniform susceptibility $\boldsymbol{\chi}^{\mathrm{C}}$ as described by Equation (11).

The Lorentzian tensor $\mathbf{L}^{\mathrm{S}}$ is

$$\mathbf{L}^{\mathrm{S}}=-\frac{1}{\zeta^{\mathrm{W}}}\int\frac{d\boldsymbol{k}}{(2\pi)^3}\boldsymbol{\Upsilon}(\boldsymbol{k})\left(v^{\mathrm{MW}}(\boldsymbol{k})+v^{\mathrm{S}}(\boldsymbol{k})+v^{\mathrm{C}}(\boldsymbol{k})\right)\chi^{\mathrm{S}}(-\boldsymbol{k}),\quad(\text{spheres are sources}). \tag{15}$$

Here the Lorentzian tensor $\mathbf{L}^{\mathrm{S}}$ describes the measured Larmor frequency shifts inside $\mathcal{M}$ from all the spheres with uniform susceptibility $\chi^{S}(\boldsymbol{k})=\chi^{\mathrm{A}}v^{\mathrm{A}}(\boldsymbol{k})+\chi^{\mathrm{M}}v^{\mathrm{M}}(\boldsymbol{k})+\chi^{\mathrm{E}}v^{\mathrm{E}}(\boldsymbol{k})$. Notice that $\mathbf{L}^{\mathrm{S}}$ depends only on structural correlation functions taking scalar values, which mean it consists of a sum of demagnetization tensors $\mathbf{N}$, Equation (5). In contrast, $\mathbf{L}^{\mathrm{C}}$ depends on tensor-valued magneto-structural correlation functions. As shown in Supporting Information S1, these correlation functions are constructed from the indicator functions and magnetic susceptibilities of cylinders and spheres in k-space. We present our main results below, while the complete (but rather lengthy) derivation can be found in the Supporting information along with numerical simulations for validation of the analytical results.

2.4.1 | Cylindrical inclusions

Consider the indicator function for a single multi-layered cylinder $v(\boldsymbol{k})$ in k-space (see Supporting Information S1) positioned at $\boldsymbol{u}$ and pointing along $\hat{\boldsymbol{n}}$. Letting r_q, R_q denote the inner and outer radii for the qth cylinder layer, respectively, $v(\boldsymbol{k})$ becomes

$$v(\boldsymbol{k})=e^{i\boldsymbol{k}\cdot\boldsymbol{u}}\frac{4\pi^2}{k}\sum_q\left(R_qJ_1(R_qk)-r_qJ_1(r_qk)\right)\delta(\boldsymbol{k}\cdot\hat{\boldsymbol{n}}),\quad(\text{multi-layered cylinder}). \tag{16}$$

The non-uniform susceptibility tensor $\boldsymbol{\chi}^{\mathrm{C}}(\boldsymbol{k})$ for a single multi-layered cylinder in k-space is found to be

$$\begin{aligned}\boldsymbol{\chi}^{\mathrm{C}}(\boldsymbol{k})=4\pi^2\delta(\boldsymbol{k}\cdot\hat{\boldsymbol{n}})e^{i\boldsymbol{k}\cdot\boldsymbol{u}}\Bigg\{&\boldsymbol{\chi}_0\sum_q\left(\xi_0(kR_q)-\xi_0(kr_q)\right)\\&-\mathrm{Re}\left\{\boldsymbol{\chi}_2e^{2i\psi}\right\}\sum_q\left(\xi_2(kR_q)-\xi_2(kr_q)\right)\Bigg\},\quad(\text{multi-layered cylinder}).\end{aligned} \tag{17}$$

Here

$$\boldsymbol{\chi}_0=\chi^{\mathrm{C}}\mathbf{I}+\frac{1}{2}\Delta\chi\left(\frac{1}{3}\mathbf{I}-\hat{\boldsymbol{n}}\hat{\boldsymbol{n}}^{\mathrm{T}}\right)\text{ and }\boldsymbol{\chi}_2=\frac{\Delta\chi}{2}\left(\hat{\boldsymbol{u}}\hat{\boldsymbol{u}}^{\mathrm{T}}-\hat{\boldsymbol{v}}\hat{\boldsymbol{v}}^{\mathrm{T}}-i\left(\hat{\boldsymbol{u}}\hat{\boldsymbol{v}}^{\mathrm{T}}+\hat{\boldsymbol{v}}\hat{\boldsymbol{u}}^{\mathrm{T}}\right)\right) \tag{18}$$

corresponds to the only non-zero coefficient matrices of the Fourier series of $\boldsymbol{\chi}^{\mathrm{C}}(\boldsymbol{k})$, and ψ denotes the azimuthal angle in the local coordinate system coaxial to the cylinder orientation $\hat{\boldsymbol{n}}$. If $\Delta\chi=0$, $\boldsymbol{\chi}^{\mathrm{C}}(\boldsymbol{k})=\boldsymbol{\chi}^{\mathrm{C}}v(\boldsymbol{k})$, which has already been considered in previous studies.[9] The magnetic

10991492, 2024, 8, Downloaded from https://analyticalsciencejournals.onlinelibrary.wiley.com/doi/10.1002/nbm.5150 by Cochrane Portugal, Wiley Online Library on [09/01/2025]. See the Terms and Conditions (https://onlinelibrary.wiley.com/terms-and-conditions) on Wiley Online Library for rules of use; OA articles are governed by the applicable Creative Commons License

susceptibility of multiple cylinders is then simply a sum over all cylinders. The bulk susceptibility $\bar{\chi}^C$ used in the macroscopic contribution $\bar{\Omega}^{\text{Macro}}$, Equation (8), is

$$\bar{\chi}^C = \bar{\chi}^C \mathbf{I} + \frac{\Delta\bar{\chi}}{2}\left(\frac{1}{3}\mathbf{I} - \mathbf{T}\right), \tag{19}$$

which follows simply from summing over all cylinders labelled by the index q, $\bar{\chi}^C = \sum_q \chi_{0q}(\boldsymbol{k}=0)/|\mathcal{M}|$. The parameters $\bar{\chi}^C = \zeta^C\chi^C$ and $\Delta\bar{\chi} = \zeta^C\Delta\chi$ define the orientationally invariant bulk magnetic susceptibilities. Here $\mathbf{T} = \sum_j \hat{\boldsymbol{n}}\hat{\boldsymbol{n}}^{\mathsf{T}}/N$ is the scatter matrix of the fiber orientation distribution function (fODF),[9,61] and is a rank-2 tensor describing the orientation dispersion of the fODF. Hence, the effective susceptibility anisotropy $\Delta\bar{\chi}$ on the mesoscopic scale depends on the fODF and the amount of orientation dispersion.

2.4.2 | Spherical inclusions

The k-space indicator function of a generic sphere $v(\boldsymbol{k})$ with radius R and positioned at $\boldsymbol{u}$ is (see Supporting Information S2)

$$\nu(\boldsymbol{k}) = e^{i\boldsymbol{k}\cdot\boldsymbol{u}} 4\pi R^3 \frac{j_1(kR)}{kR}, \quad (\text{generic sphere}). \tag{20}$$

Hence, to determine the model-predicted Larmor frequency shift $\bar{\Omega}$, all we need to do is compute the two tensors $\mathbf{L}^C$ and $\mathbf{L}^S$ using the derived indicator functions. The integrals describing the Lorentzian tensors are included as Supporting information. The next section presents the results for $\mathbf{L}^C$ and $\mathbf{L}^S$.

2.5 | Mesoscopic Larmor frequency shift of WM magnetic microstructure model

In this section, we provide the final analytical results for the mesoscopic Larmor frequency shift $\bar{\Omega}$ from all the different inclusions. The main results are presented separately for the contribution induced by cylinders with susceptibility χ^C ($\mathbf{L}^C$, cf. Equation (14)), and the contribution generated by spheres with susceptibility χ^S ($\mathbf{L}^S$, cf. Equation (15)).

2.5.1 | Larmor frequency shift from cylindrical inclusions

For a distribution of multi-layered cylinders, we find for the Lorentzian tensor $\mathbf{L}^C$ (cf. Equation (14))

$$\mathbf{L}^C = -\bar{\chi}^C\frac{1}{2}\left(\mathbf{T} - \frac{1}{3}\mathbf{I}\right) + \Delta\bar{\chi}\frac{1}{12}\left((1-\lambda)\mathbf{T} + \left(\lambda + \frac{1}{3}\right)\mathbf{I}\right). \tag{21}$$

Here λ is a geometric factor (see Equations (S21) and (S65) in Supporting information) depending on the layer geometry of the axons and their internal water fractions. Equation (21) is valid whether MW is relaxed or not, but its saturation state is reflected in the value of λ. For example, in the case of fully relaxed MW and axons of similar sizes with many thin layers,[14]

$$\lambda = -6\frac{\zeta^{\text{AW}}}{\zeta^C\zeta^{\text{W}}}\frac{d}{d+d^{\text{W}}}\ln(g) > 0, \quad (\text{equally sized cylinder layers}), \tag{22}$$

where ζ^{AW} is the intra-axonal water volume fraction, $g = r_1/R_N$ is the ratio between the radii of the inner r_1 and outer cylinder layers R_N, d is the width of the lipid layers and d^{W} the width of the MW layers. This means that cell bodies, neurofilaments, microtubules, and so on that can be found in the intra-axonal space decrease λ, due to the sensitivity to ζ^{AW}. This is because the mesoscopic frequency shift, cf. Equation (3), is considered here over all the water inside $\mathcal{M}$, which is normalized by the water volume fraction ζ^{W}. Hence, it is obvious that the less water there is present in the intra-axonal space, the less it contributes to the mesoscopic frequency shift $\bar{\Omega}(\mathbf{R})$. If the cylinders have different sizes, Equation (S65) in Supporting information must be averaged according to the size distribution.[62]

The scatter matrix $\hat{\mathbf{B}}^{\mathsf{T}}\mathbf{T}\hat{\mathbf{B}}$ along the measured direction $\hat{\mathbf{B}}$, cf. Equation (2), can be estimated using dMRI via the relation[24,63]

10991492, 2024, 8, Downloaded from https://analyticalsciencejournals.onlinelibrary.wiley.com/doi/10.1002/nbm.5150 by Cochrane Portugal, Wiley Online Library on [09/01/2025]. See the Terms and Conditions (https://onlinelibrary.wiley.com/terms-and-conditions) on Wiley Online Library for rules of use; OA articles are governed by the applicable Creative Commons License

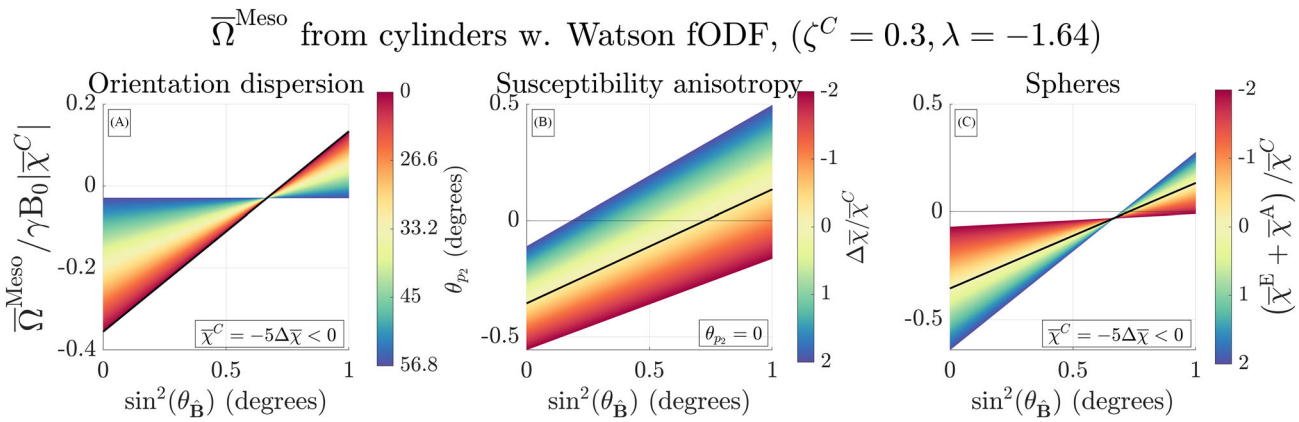

FIGURE 4 Mesoscopic frequency shift $\overline{\Omega}^{\text{Meso}}$ from cylinders and spheres with axially symmetric dispersion and anisotropic susceptibility. **A**, $\overline{\Omega}^{\text{Meso}}$ only for cylinders, with susceptibility described by the legend and for varying angles $\sin^2\left(\theta_{\widehat{\mathbf{B}}}\right)$ between the external field and fODF symmetry axis. Colors represent the dispersion angles. As the dispersion increases, the frequency variation is dampened with a fixed focal point at the magic angle. **B**, Variation in the ratio between the isotropic $\overline{\chi}^C$ and anisotropic magnetic susceptibility $\Delta\overline{\chi}$, indicated by the colors. Here, the dispersion is set to 0 (parallel cylinders). $\Delta\overline{\chi}$ mainly shifts the Larmor frequency up or down. **C**, Change in the mesoscopic frequency for a non-zero spherical magnetic susceptibility $\overline{\chi}^E + \overline{\chi}^A$. Here the spherical susceptibility changes the slope but keeps the focal point fixed at the magic angle. The black lines in **A–C** indicate the same configuration across figures.

$$\mathbf{T} - \frac{1}{3}\mathbf{I} = \frac{2}{15}\sum_{m=-2}^{2} p_{2m}\mathcal{Y}_{2m}, \tag{23}$$

where $\mathcal{Y}_{2m}$ defines the $l=2$ symmetric trace-free representation of the rotation group SO(3)[63] and the p_{2m} denote the Laplace expansion coefficients of the fODF normalized such that the fODF integrates to 1. This normalization differs from our previous study[9] by a factor of 1/5, and is chosen for later convenience. Notice that only p_{2m} and $l=2$ spherical harmonics Y_2^m, corresponding to the truncated Laplace expansion of the fODF, appear in Equation (23). If $\Delta\overline{\chi}=0$, our previously published result for dispersed cylinders with scalar susceptibility[9] is obtained. The orientation dependence of the mesoscopic contribution to $\mathbf{L}^C$ proportional to $\Delta\overline{\chi}$ (second term in Equation (21)) is embodied by a tensor with non-zero trace, in contrast to the tensor associated with the $\overline{\chi}^C$ contribution (first term in Equation (21)), which has zero trace. When dispersion is uniform, the scatter matrix $\mathbf{T}$ is equal to the identity $\mathbf{T}=\mathbf{I}/3$, which nulls the contribution from $\overline{\chi}^C$ such that $\mathbf{L}^C = \mathbf{I}\Delta\overline{\chi}(1+\lambda)/18$. Hence, the model predicts a non-zero frequency shift even for uniform orientation dispersion (see Figure 4) due to $\Delta\overline{\chi}$.

Using Equations (8) and (19), the macroscopic contribution from the cylinders can be approximated on the scale of the MRI sampling resolution to be

$$\overline{\Omega}^{\text{Macro}}(\mathbf{R}) = \gamma B_0 \widehat{\mathbf{B}}^{\mathsf{T}} \sum_{\mathbf{R}'} \overline{\Upsilon}(\mathbf{R}-\mathbf{R}')\left(\overline{\chi}^C(\mathbf{R}') + \frac{\Delta\overline{\chi}(\mathbf{R}')}{2}\left(\frac{1}{3}\mathbf{I} - \mathbf{T}(\mathbf{R}')\right)\right)\widehat{\mathbf{B}}, \quad \text{(from cylinders)}. \tag{24}$$

Equation (24) describes how $\Delta\overline{\chi}$ gives rise to a macroscopic orientation dependence of the cylinders. The bulk susceptibility tensor, which STI aims to quantify,[64] thus depend on the fODF of WM axons. It is only in the limit of uniformly dispersed cylinders that the $\Delta\overline{\chi}$ term vanishes. This means that the apparent susceptibility anisotropy in the macroscopic contribution depends on the distribution of axons and the degree of orientation dispersion on the mesoscopic scale.

2.5.2 | Larmor frequency shift from spherical inclusions

The contribution from spheres to the Larmor frequency is derived in Supporting Information S2. When the spheres occupy a low volume fraction, the Lorentzian tensor $\mathbf{L}^S$, Equation (15), is found to be

$$\mathbf{L}^S = \frac{1}{2}\left(-\overline{\chi}^M + (\overline{\chi}^E + \overline{\chi}^A)\frac{\zeta^C}{\zeta^W}\right)\left(\mathbf{T} - \frac{1}{3}\mathbf{I}\right). \tag{25}$$

10991492, 2024, 8, Downloaded from https://analyticalsciencejournals.onlinelibrary.wiley.com/doi/10.1002/nbm.5150 by Cochrane Portugal, Wiley Online Library on [09/01/2025]. See the Terms and Conditions (https://onlinelibrary.wiley.com/terms-and-conditions) on Wiley Online Library for rules of use; OA articles are governed by the applicable Creative Commons License

Equation (25) reflects the anisotropic mesoscopic contribution that emerges, because the reporting MR fluid and spherical inclusions are spatially restricted due to the presence of the cylinders. We only include contributions up to first order in sphere volume fraction in Equation (25). However, $\mathbf{L}^S$ also includes contributions that are second order in sphere volume fraction. For high volume fraction of spheres, the full result is found in Equation (S63) in Supporting information. If we assume a volume fractions of axons around $\zeta^C \sim 0.35$ then the ratio $\zeta^C/\zeta^W \sim 0.5$. This means that positively magnetized extra-axonal (e.g. iron) and intra-axonal sources with susceptibility $\overline{\chi}^E + \overline{\chi}^A > 0$ can produce a mesoscopic frequency shift of the same order of magnitude as $\overline{\chi}^C < 0$, if $-\overline{\chi}^C \sim \overline{\chi}^E + \overline{\chi}^A$. Hence, we cannot conclude that an orientation-dependent Larmor frequency shift originates from the cylinders, as it could just as well reflect, for example, iron or intra-axonal sources.[11,14] The contribution from $\overline{\chi}^M$ (spheres in MW) in Equation (25) generates a contribution to the Lorentzian tensor $\mathbf{L}^S$ similar to that of $\overline{\chi}^C$ to $\mathbf{L}^C$ in Equation (21). Therefore, $\overline{\chi}^C$ can in practice be considered an effective susceptibility of both the cylinder layers (lipids) and spheres in MW (e.g. MBP).

The macroscopic contribution from spheres is

$$\overline{\Omega}^{\text{Macro}}(\mathbf{R}) = \gamma B_0 \sum_{\mathbf{R}'} \widehat{\mathbf{B}}^{\mathsf{T}} \overline{\mathbf{Y}}(\mathbf{R}-\mathbf{R}') \widehat{\mathbf{B}} \overline{\chi}^S(\mathbf{R}'), \quad (\text{from spheres}). \tag{26}$$

Here $\overline{\chi}^S$ defines the bulk susceptibility of all spherical inclusions, and does not depend on their anisotropic arrangement, similarly to $\overline{\chi}^C$ in Equation (24).

2.5.3 | Total mesoscopic frequency shift $\overline{\Omega}^{\text{Meso}}$

By combining Equations (21) and (25), the total mesoscopic contribution $\overline{\Omega}^{\text{Meso}}(\mathbf{R})$ to the mesoscopically averaged Larmor frequency shift $\overline{\Omega}(\mathbf{R})$, Equation (2), from both cylinders and spheres becomes

$$\begin{aligned}\overline{\Omega}^{\text{Meso}}(\mathbf{R}) = &-\left(\overline{\chi}^C + \overline{\chi}^M - \left(\overline{\chi}^E + \overline{\chi}^A\right)\frac{\zeta^C}{\zeta^W}\right)\frac{1}{2}\left(\widehat{\mathbf{B}}^{\mathsf{T}}\mathbf{T}\widehat{\mathbf{B}} - \frac{1}{3}\right) \\ &+ \frac{\Delta\overline{\chi}}{12}\left(\widehat{\mathbf{B}}^{\mathsf{T}}\mathbf{T}\widehat{\mathbf{B}}(1-\lambda) + \left(\lambda + \frac{1}{3}\right)\right).\end{aligned} \tag{27}$$

Equation (27) describing the mesoscopic frequency shift from both cylinders and spheres is our main theoretical result in this study, and reduces to our previous result[9] when $\overline{\chi}^C$ is the only non-zero magnetic susceptibility.

2.5.4 | $\overline{\Omega}^{\text{Meso}}$ for axially symmetric fODF

If the fODF is axially symmetric, only $Y_2^0\left(\widehat{\mathbf{B}}\right)$ contributes to the mesoscopic frequency shift in Equation (27). In this case

$$\overline{\Omega}^{\text{Meso}} = a\sin^2\left(\theta_{\mathbf{B}}\right) + b, \quad (\text{axially symmetric fODF}), \tag{28}$$

where

$$a = \frac{1}{2}\gamma B_0\left(\overline{\chi}^C + \overline{\chi}^M - \left(\overline{\chi}^E + \overline{\chi}^A\right)\frac{\zeta^C}{\zeta^W} - \frac{1}{6}\Delta\overline{\chi}(1-\lambda)\right)p_2 \tag{29}$$

$$b = \gamma B_0 \frac{1}{3}\left(-p_2\left(\overline{\chi}^C + \overline{\chi}^M - \left(\overline{\chi}^E + \overline{\chi}^A\right)\frac{\zeta^C}{\zeta^W}\right) + \Delta\overline{\chi}\frac{1}{6}\left((1+\lambda) + p_2(1-\lambda)\right)\right). \tag{30}$$

The angle $\theta_{\mathbf{B}}$ is the angle between the field and symmetry axis of the fODF. Here

$$p_2 = \sqrt{\frac{1}{20\pi}\sum_{m=-2}^{2}|p_{2m}|^2} \in [0,1] \tag{31}$$

10991492, 2024, 8, Downloaded from https://analyticalsciencejournals.onlinelibrary.wiley.com/doi/10.1002/nbm.5150 by Cochrane Portugal, Wiley Online Library on [09/01/2025]. See the Terms and Conditions (https://onlinelibrary.wiley.com/terms-and-conditions) on Wiley Online Library for rules of use; OA articles are governed by the applicable Creative Commons License

is the $l=2$ rotation invariant of the fODF,[65,66] which serves as a natural attenuation factor for the orientation-dependent $\sin^2\left(\theta_{\widehat{\mathbf{B}}}\right)$ term due to orientation dispersion. This is qualitatively similar but quantitatively different from the fractional anisotropy (FA) of the diffusion tensor, which has been proposed in previous studies.[23]

Figure 4A,B shows $\overline{\Omega}^{\text{Meso}}/\gamma B_0|\overline{\chi}^{\text{C}}|$ only from cylinders with orientations following a Watson fODF.[67] Here the volume fraction is $\zeta^{\text{C}}=0.3$, $\zeta^{\text{W}}=0.7$, $g=0.65$, $d/\left(d+d^{\text{W}}\right)=2/3$ and $\zeta^{\text{AW}}=0.2$, resulting in $\lambda=1.6$. Figure 4A demonstrates the effect of increased dispersion when $\Delta\overline{\chi}=-\overline{\chi}^{\text{C}}/5$, as chosen based on previous findings.[23] Dispersion is here quantified by a dispersion angle[65] θ_{p_2} ranging from 0° up to the magic angle $\theta_{\text{MA}}\approx 54.7^\circ$, where the dispersion effect will be maximum. Here, a non-zero frequency shift remains present due to non-zero susceptibility anisotropy $\Delta\overline{\chi}$ in the limit of fully dispersed cylinders ($p_2=0$). Figure 4B shows the effect when varying $\Delta\overline{\chi}/\overline{\chi}^{\text{C}}$, where the main effect is to shift $\overline{\Omega}^{\text{Meso}}/\gamma B_0|\overline{\chi}^{\text{C}}|$ up or down. The effect on the slope depends on how much λ differs from 1; cf. Equation (29). Figure 4C shows $\overline{\Omega}^{\text{Meso}}/\gamma B_0|\overline{\chi}^{\text{C}}|$ for a non-zero spherical susceptibility $(\overline{\chi}^{\text{A}}+\overline{\chi}^{\text{E}})/\overline{\chi}^{\text{C}}$. The slope of $\overline{\Omega}^{\text{Meso}}/\gamma B_0|\overline{\chi}^{\text{C}}|$ changes substantially when the spherical susceptibility is comparable to $|\overline{\chi}^{\text{C}}|$.

2.5.5 | $\overline{\Omega}^{\text{Meso}}$ for a non-axially symmetric fODF

To understand the effect of having a non-axially symmetric fODF, we assume for simplicity that susceptibility anisotropy is zero, $\Delta\chi=0$, in this section. Consider first Equation (28) for an axially symmetric fODF, where $\Delta\chi=0$ implies $a=\gamma B_0\overline{\chi}_{\text{eff}}p_2/2$ and $b=-\gamma B_0\overline{\chi}_{\text{eff}}p_2/3$. Here, $\overline{\chi}_{\text{eff}}$ denotes the effective susceptibility $\overline{\chi}_{\text{eff}}=\left(\overline{\chi}^{\text{C}}+\overline{\chi}^{\text{M}}-\left(\overline{\chi}^{\text{E}}+\overline{\chi}^{\text{A}}\right)\zeta^{\text{C}}/\zeta^{\text{W}}\right)$. Hence, $\overline{\Omega}^{\text{Meso}}\left(\theta_{\widehat{\mathbf{B}}}\right)=\gamma B_0\overline{\chi}_{\text{eff}}p_2\left(\sin^2(\theta_B)/2-1/3\right)$ will always be zero when $\theta_{\widehat{\mathbf{B}}}$ is equal to the magic angle $\theta_{\text{MA}}\simeq 54.7^\circ$. This is demonstrated in Figure 5A for the Watson distribution[67] with $\widehat{\boldsymbol{z}}$ as symmetry axis and with dispersion angle[68] θ_{p_2} ranging from 5.7° to θ_{MA}. All curves cross 0 (black dotted line) at θ_{MA}, while increasing dispersion attenuates the slope of the frequency shift versus $\sin^2\theta_B$. To examine the effect of having a non-axially symmetric fODF, the Bingham distribution[67] with dispersion axes along $\widehat{\boldsymbol{x}}$ and $\widehat{\boldsymbol{y}}$ was used as fODF in Figure 5B–D. The dispersion angle $\theta_{\widehat{x}}$ along $\widehat{\boldsymbol{x}}$ is fixed at 5.7°, while dispersion $\theta_{\widehat{y}}$ is varied from 5.7° to θ_{MA}. When the dispersions along $\widehat{\boldsymbol{x}}$ and $\widehat{\boldsymbol{y}}$ are equal, the Bingham fODF reduces to the Watson fODF. Since the trace of the scatter matrix is unity, $\text{Tr}[\mathbf{T}]=1$, increasing dispersion along $\widehat{\boldsymbol{y}}$ by an angle $\theta_{\widehat{y}}$ results in increasing the eigenvalue of $\mathbf{T}$ corresponding to the eigenvector along $\widehat{\boldsymbol{y}}$, while the corresponding eigenvalue to $\widehat{\boldsymbol{z}}$ decreases due to conservation of trace of $\mathbf{T}$ (since dispersion along $\widehat{\boldsymbol{x}}$ is small, we can neglect any change in its eigenvalue of $\mathbf{T}$ after varying $\widehat{\boldsymbol{y}}$). In Figure 5B, the field is rotated in the $\widehat{\boldsymbol{x}}\widehat{\boldsymbol{z}}$ plane. Here the focal point appears at 90°, and the zero-frequency angle now becomes a decreasing function of dispersion. In Figure 5C, the field is at an equal azimuthal angle to the two dispersion axes, which makes the frequency shift appear axially symmetric, as the zero-crossing is at θ_{MA} again. Finally, in Figure 5D, the field is tilted in the $\widehat{\boldsymbol{y}}\widehat{\boldsymbol{z}}$ plane. The zero-frequency angle is now shifted to the right as both the frequency slope and offset are reduced. As a consequence, this means that non-axially symmetric dispersion can mimic the effect of susceptibility anisotropy, and only by knowing the fODF it is possible to discern the actual susceptibility anisotropy.

3 | METHODS

3.1 | Simulations

We designed two sets of simulations to (a) validate the analytical result, Equation (21), and (b) demonstrate the feasibility of solving the inverse problem and extract susceptibility parameters from frequency measurements. All simulations were done in MATLAB (MathWorks, Natick, MA, USA). The data that support the findings of this study are available from the corresponding author upon reasonable request.

3.1.1 | Simulation (a): validity of the Lorentzian tensor for a distribution of cylinders with susceptibility anisotropy $\Delta\chi$

A total of 11 unique samples of non-overlapping cylindrical shells with varying orientation dispersion were constructed to validate the model. The sample is represented by a cubic volume with side lengths L. Figure 6 gives an overview of the sample geometries. The radii of the cylinders ρ were drawn from a gamma distribution with mean and standard deviation (SD) 0.0143L, and the g-ratio, the ratio between the inner and outer radii, was fixed at $g=0.65$.[69] The positions were drawn from a uniform distribution. The total volume fraction achieved this way was $\zeta\approx 0.15$, and $\lambda\approx 2.2$. Dispersion was generated from an axially symmetric and uniform distribution of orientations $\widehat{\boldsymbol{n}}$, within an allowed polar range $\cos^{-1}(\widehat{\boldsymbol{z}}\cdot\widehat{\boldsymbol{n}})=\theta<\theta_c$, where θ_c is the cut-off angle. Every sample was discretized in a 3D grid, with a resolution set by the number of grid points. This defined the indicator function $v^{\text{C}}(\boldsymbol{r})$ of the cylinders on the discretized grid. The susceptibility tensor $\chi^{\text{C}}(\boldsymbol{r})$ was generated using Equation (S6) in Supporting information. This required calculating the azimuthal angles in local coordinates and orientation for each cylinder on

10991492, 2024, 8, Downloaded from https://analyticalsciencejournals.onlinelibrary.wiley.com/doi/10.1002/nbm.5150 by Cochrane Portugal, Wiley Online Library on [09/01/2025]. See the Terms and Conditions (https://onlinelibrary.wiley.com/terms-and-conditions) on Wiley Online Library for rules of use; OA articles are governed by the applicable Creative Commons License

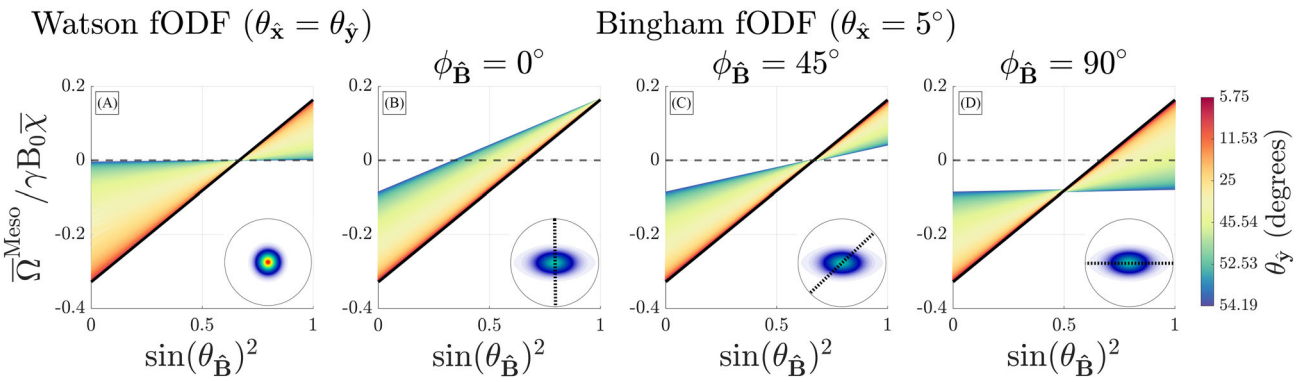

FIGURE 5 Mesoscopic frequency shift from cylinders with orientation dispersion and scalar susceptibility. **A**, $\overline{\Omega}^{\text{Meso}}$ for an axially symmetric Watson distribution, as a function of the angle $\theta_{\hat{\mathbf{B}}}$ between the applied field and the symmetry axis of the cylinders' fODF. The colors encode the dispersion angle, as indicated by the color bar to the right. As the dispersion increases, the mesoscopic frequency is dampened. **B–D**, $\overline{\Omega}^{\text{Meso}}$ for a non-axially symmetric Bingham distribution with axes $\hat{\boldsymbol{x}}$ and $\hat{\boldsymbol{y}}$ and with a fixed dispersion angle $\theta_{\hat{\boldsymbol{x}}} = 5°$, while the colors encode the dispersion angle $\theta_{\hat{\boldsymbol{y}}}$. Mesoscopic frequency versus tilt angle $\theta_{\hat{\mathbf{B}}}$ in the *zx* plane ($\phi_{\hat{\mathbf{B}}} = 0°$) indicated by the dashed line (**B**), in the *zy* plane ($\phi_{\hat{\mathbf{B}}} = 90°$) (**D**), and in between ($\phi_{\hat{\mathbf{B}}} = 45°$) (**C**). The black lines indicate the same fODF across all four figures.

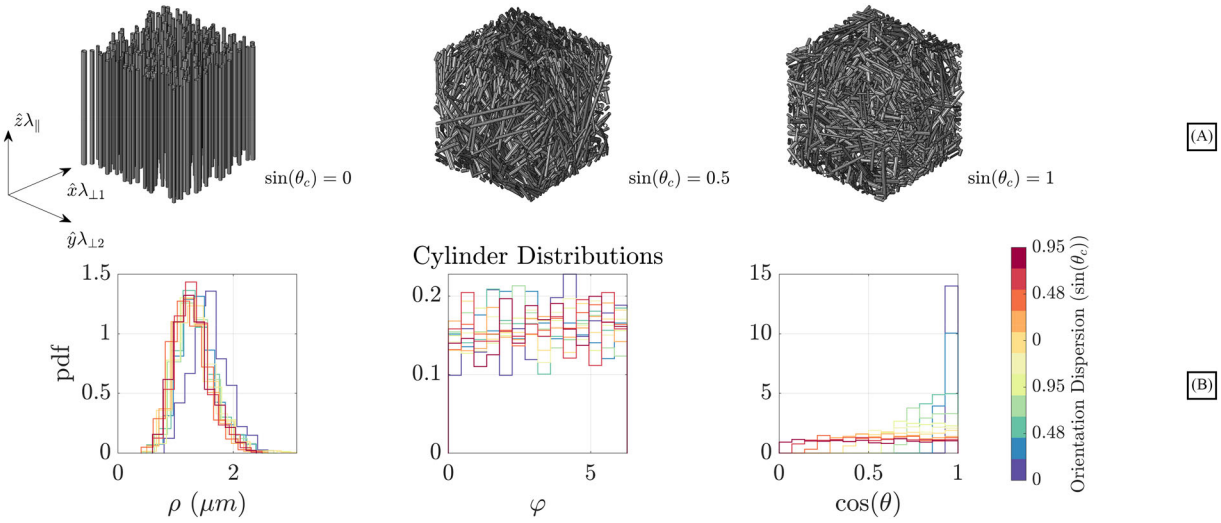

FIGURE 6 Simulation (a). **A**, Populations of cylinders with different levels of orientation dispersion. **B**, Probability density function (pdf) of the resulting cylinder parameters for each configuration. The cylinder radius ρ is gamma-distributed, while θ and φ are uniformly distributed in the full range of azimuthal angle and from zero to the maximum polar angle θ_c, respectively. Colors are used to represent different populations with orientation dispersion indicated by the color bar.

the 3D grid to compute the susceptibility tensor in the laboratory frame. Susceptibilities were chosen to be maximally anisotropic by setting $\chi^{\mathsf{C}} = \Delta\chi/3$, c.f. Equation (8), as previous simulations[9] had already validated the isotropic contribution. Using a discrete Fourier transform with periodic boundaries, $v^{\mathsf{C}}(\boldsymbol{k})$, $\chi^{\mathsf{C}}(\boldsymbol{k})$, and in turn the correlation tensor $\boldsymbol{\Gamma}(\boldsymbol{k})$, Equation (S2) in Supporting information, were computed. From this, the normalized Lorentzian tensor $\mathbf{L}/[\zeta\Delta\chi(1+\lambda)/6]$ could be estimated solely from susceptibility anisotropy using Equation (S1), and compared with the model prediction $\frac{1}{2}(\mathbf{I}-\mathbf{T})$, cf. Equation (17). The eigenvalues $(\lambda_{\perp 1}, \lambda_{\perp 2}, \lambda_{\parallel})$ of $\mathbf{L}/[\zeta\Delta\chi(1+\lambda)/6]$ were calculated for both simulation and model prediction and compared for each population.

3.1.2 | Simulation (b): feasibility of solving inverse problem

Estimating the magnetic susceptibility $\vec{\chi}$ from the MRI measured Larmor frequency shift amounts to solving the linear system of equations $\vec{\Omega}_{\text{MRI}} = \mathbf{A}\vec{\chi}$ (here vectors indicate a vectorization over the voxels):

10991492, 2024, 8, Downloaded from https://analyticalsciencejournals.onlinelibrary.wiley.com/doi/10.1002/nbm.5150 by Cochrane Portugal, Wiley Online Library on [09/01/2025]. See the Terms and Conditions (https://onlinelibrary.wiley.com/terms-and-conditions) on Wiley Online Library for rules of use; OA articles are governed by the applicable Creative Commons License

$$\begin{pmatrix} \vec{\Omega}_{\mathrm{MRI}}\left(\hat{\mathbf{B}}_1\right) \\ \vec{\Omega}_{\mathrm{MRI}}\left(\hat{\mathbf{B}}_2\right) \\ \vdots \\ \vec{\Omega}_{\mathrm{MRI}}\left(\hat{\mathbf{B}}_n\right) \end{pmatrix} = \gamma B_0 \begin{pmatrix} \mathbf{A}^{\chi^C}\left(\hat{\mathbf{B}}_1\right) & \mathbf{A}^{\Delta\chi}\left(\hat{\mathbf{B}}_1\right) & \mathbf{A}^{\lambda\Delta\chi}\left(\hat{\mathbf{B}}_1\right) & \mathbf{A}^{\chi^S}\left(\hat{\mathbf{B}}_1\right) \\ \mathbf{A}^{\chi^C}\left(\hat{\mathbf{B}}_2\right) & \mathbf{A}^{\Delta\chi}\left(\hat{\mathbf{B}}_2\right) & \mathbf{A}^{\lambda\Delta\chi}\left(\hat{\mathbf{B}}_2\right) & \mathbf{A}^{\chi^S}\left(\hat{\mathbf{B}}_2\right) \\ \vdots & \vdots & \vdots & \vdots \\ \mathbf{A}^{\chi^C}\left(\hat{\mathbf{B}}_n\right) & \mathbf{A}^{\Delta\chi}\left(\hat{\mathbf{B}}_n\right) & \mathbf{A}^{\lambda\Delta\chi}\left(\hat{\mathbf{B}}_n\right) & \mathbf{A}^{\chi^S}\left(\hat{\mathbf{B}}_n\right) \end{pmatrix} \begin{pmatrix} \vec{\chi}^C \\ \overrightarrow{\Delta\chi} \\ \overrightarrow{\lambda\Delta\chi} \\ \vec{\chi}^S \end{pmatrix}. \tag{32}$$

The vector $\vec{\chi} = \left(\vec{\chi}^C \;\; \overrightarrow{\Delta\chi} \;\; \overrightarrow{\lambda\Delta\chi} \;\; \vec{\chi}^S\right)^{\mathsf{T}}$ is a $4N \times 1$ block vector in voxel space containing the four main bulk susceptibilities, where N is the number of voxels. $\vec{\Omega}_{\mathrm{MRI}}$ has dimensions $n\mathrm{N} \times 1$ for n unique sampling orientations $\hat{\mathbf{B}}$. Each $\mathbf{A}^{(i)}\left(\hat{\mathbf{B}}\right)$ is an $N \times N$ matrix in voxel space where every element includes a tensor contraction with $\hat{\mathbf{B}}$ describing the magnetic response, which is here referred to as magnetic space to distinguish the two. $\overline{\chi}^S$ is assumed to be small such that its mesoscopic contribution, Equation (25), can be neglected. The elements $\mathrm{A}^{(i)}\left(\mathbf{R}_i,\mathbf{R}_j\right)$ of every block matrix $\mathbf{A}^{(i)}\left(\hat{\mathbf{B}}\right)$, for a row in the response matrix $\mathbf{A}$, can be represented as

$$\begin{aligned} \mathrm{A}^{\chi^C}\left(\mathbf{R}_i,\mathbf{R}_j\right) &= \mathrm{M}(\mathbf{R}_i)\hat{\mathbf{B}}^{\mathsf{T}}\left[-\frac{1}{2}\mathbf{T}(\mathbf{R}_j) + \frac{1}{3}\mathbf{I} + \overline{\mathbf{Y}}(\mathbf{R}_i - \mathbf{R}_j)\right]\hat{\mathbf{B}}\mathrm{M}(\mathbf{R}_j) \\ \mathrm{A}^{\lambda\Delta\chi}\left(\mathbf{R}_i,\mathbf{R}_j\right) &= \frac{1}{12}\mathrm{M}(\mathbf{R}_i)\hat{\mathbf{B}}^{\mathsf{T}}\left[\mathbf{I} - \mathbf{T}(\mathbf{R}_j)\right]\hat{\mathbf{B}}\mathrm{M}(\mathbf{R}_j) \\ \mathrm{A}^{\Delta\chi}\left(\mathbf{R}_i,\mathbf{R}_j\right) &= -\frac{1}{2}\mathrm{M}(\mathbf{R}_i)\hat{\mathbf{B}}^{\mathsf{T}}\left[\overline{\mathbf{Y}}(\mathbf{R}_i - \mathbf{R}_j)\mathbf{T}(\mathbf{R}_j) - \frac{1}{3}\overline{\mathbf{Y}}(\mathbf{R}_i - \mathbf{R}_j) - \frac{1}{6}\mathbf{T}(\mathbf{R}_j) - \frac{1}{18}\mathbf{I}\right]\hat{\mathbf{B}}\mathrm{M}(\mathbf{R}_j) \\ \mathrm{A}^{\chi^S}\left(\mathbf{R}_i,\mathbf{R}_j\right) &= \mathrm{M}(\mathbf{R}_i)\hat{\mathbf{B}}^{\mathsf{T}}\overline{\mathbf{Y}}(\mathbf{R}_i - \mathbf{R}_j)\hat{\mathbf{B}}\mathrm{M}(\mathbf{R}_j). \end{aligned} \tag{33}$$

Here $\mathrm{M}(\mathbf{R}_i)$ is a diagonal mask matrix describing the spatial distribution of allowed susceptibility sources where $\vec{\Omega}_{\mathrm{MRI}}$ is successfully measured[70] (here the sample mask). The matrix dimension of the total response matrix $\mathbf{A}$ is far too great to physically allocate, which hampers the possibility of solving Equation (32) in closed form. However, $\mathbf{A}$ implements fast linear operations such as convolutions and simple matrix multiplications. For these types of linear problems of impractically high dimensionality, one may turn to iterative least squares schemes, which has the benefit of never allocating any matrices, but declares every matrix as a function handle, so only vectors of dimension equal to $\vec{\Omega}_{\mathrm{MRI}}$ and $\vec{\chi}$ are allocated. An example of such solvers is the LSMR[71] algorithm, which is used here to invert Equation (32). Using these simulations, we tested the feasibility of extracting susceptibility parameters from whole brain measurements of the MRI frequency shift $\overline{\Omega}_{\mathrm{MRI}}\left(\hat{\mathbf{B}}\right)$ acquired at multiple sample orientations $\hat{\mathbf{B}}$. This was done by generating a digital brain phantom from previously acquired data.[24] The phantom is outlined in Figure 7 and is based on dMRI measurements of an ex vivo mouse brain at 16.4 T. The brain was measured with a matrix size of $102 \times 102 \times 170$ and was segmented into gray matter (GM) and WM from $b = 0$ ms/μm^2 images using statistical parametric mapping (SPM).[72] From diffusional kurtosis imaging (DKI)[73] fitting ($b = 3$, 5 ms/μm^2, 30 directions), FA and mean diffusivity (MD) was extracted from the diffusion tensor. Laplace expansion coefficients of the fODF, p_{2m}, were estimated using fiber ball imaging (FBI)[74] ($b = 10$ ms/μm^2, 75 directions). From these, maps of four orientationally invariant parameters were synthesized: $\overline{\chi}^C$, $\Delta\overline{\chi}$, $\lambda\Delta\overline{\chi}$ and $\overline{\chi}^S$. All four parameters would subsequently need to be estimated in each voxel of the whole brain. Here $\overline{\chi}^S = \overline{\chi}^S_{\mathrm{WM}} + \overline{\chi}^S_{\mathrm{GM}}$ are the bulk susceptibilities from spheres in GM and WM. The resulting Larmor frequencies from each of these "sources" are $\overline{\Omega}^{\mathrm{Meso}}_{\overline{\chi}^C}\left(\hat{\mathbf{B}}\right) + \overline{\Omega}^{\mathrm{Macro}}_{\overline{\chi}^C}\left(\hat{\mathbf{B}}\right)$, $\overline{\Omega}^{\mathrm{Meso}}_{\Delta\overline{\chi}}\left(\hat{\mathbf{B}}\right) + \overline{\Omega}^{\mathrm{Macro}}_{\Delta\overline{\chi}}\left(\hat{\mathbf{B}}\right)$, $\overline{\Omega}^{\mathrm{Meso}}_{\Delta\overline{\chi}\lambda}\left(\hat{\mathbf{B}}\right)$, and $\overline{\Omega}^{\mathrm{Macro}}_{\overline{\chi}^S}\left(\hat{\mathbf{B}}\right)$, and they are computed according to Equation (32). Their sum defines the total MRI Larmor frequency shift $\overline{\Omega}_{\mathrm{MRI}}\left(\hat{\mathbf{B}}\right)$ for each orientation $\hat{\mathbf{B}}$. Figure 7 shows the susceptibility and noiseless frequency maps. The inverse problem was solved for different numbers of sample orientations made using an electrostatic repulsion scheme,[75] adding to $\overline{\Omega}_{\mathrm{MRI}}\left(\hat{\mathbf{B}}\right)$ different levels of Gaussian noise $\varepsilon \sim N\left(0, \sigma^2/\mathrm{SNR}^2\right)$ by varying the signal-to-noise ratio (SNR), and finally, the maximum polar angle of sample rotation. The solution with the lowest root-mean-squared error (RMSE) compared with ground truth during fitting was chosen for analysis.

4 | RESULTS

4.1 | Simulations

4.1.1 | Simulation (a): validity of the Lorentzian tensor for a distribution of cylinders with susceptibility anisotropy

Figure 8 shows the eigenvalues $\left(\lambda_{\perp 1}, \lambda_{\perp 2}, \lambda_{\parallel}\right)$ of $\mathbf{L}/[\zeta\Delta\chi(1+\lambda)/6]$ and $\frac{1}{2}(\mathbf{I} - \mathbf{T})$ from all the cylinder samples with varying orientation dispersion, where $\chi^C = \Delta\chi/3$. The model predicts the same behavior as the ground truth simulation. In contrast to our previous results[9] for the Lorentzian

10991492, 2024, 8, Downloaded from https://analyticalsciencejournals.onlinelibrary.wiley.com/doi/10.1002/nbm.5150 by Cochrane Portugal, Wiley Online Library on [09/01/2025]. See the Terms and Conditions (https://onlinelibrary.wiley.com/terms-and-conditions) on Wiley Online Library for rules of use; OA articles are governed by the applicable Creative Commons License

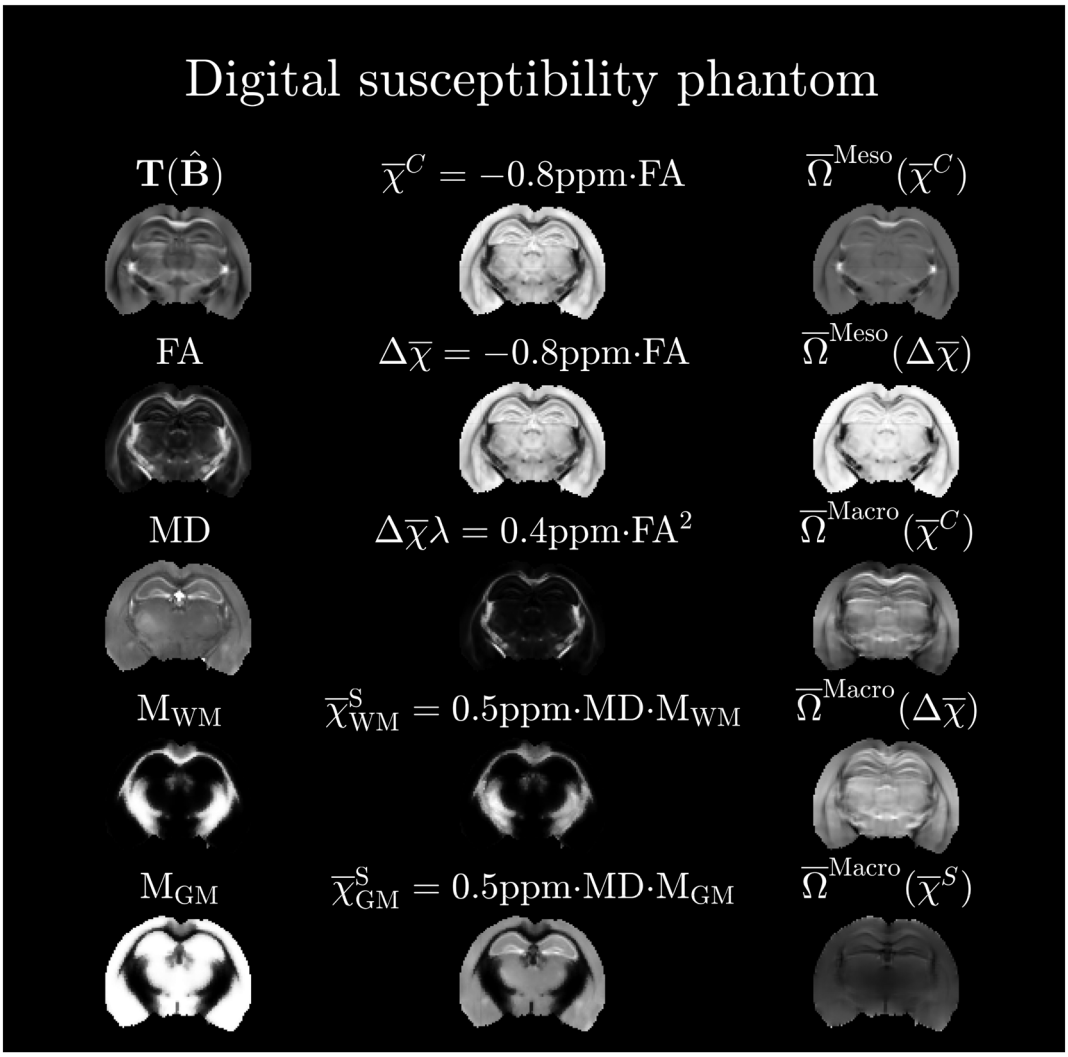

FIGURE 7 Simulation (b): digital susceptibility phantom. Left column, FA, MD, and fODF from dMRI measurement of an ex vivo mouse brain. WM and GM masks, M_{WM} and M_{GM} respectively, were extracted using SPM.[72] Middle column, ground truth susceptibility maps defined from this. Right column, Corresponding noiseless Larmor frequencies for a particular sample orientation $\widehat{\mathbf{B}}$. The sum of all frequencies defines the MRI measured frequency shift $\overline{\Omega}_{\text{MRI}}$. The aim is to estimate the susceptibility maps from the measured frequency $\overline{\Omega}_{\text{MRI}}$ acquired at multiple sample orientations and after adding noise.

tensor relating to χ^{C}, here the Lorentzian tensor from susceptibility anisotropy $\Delta\chi$ has non-zero eigenvalues for all levels of orientation dispersion. The eigenvector for $\lambda_{\|}$, corresponding to the symmetry axis of the cylinder orientation distribution, also agreed with simulations within a mean angular error of 3.5° (data not shown).

4.1.2 | Simulation (b): feasibility of solving inverse problem

Figure 9 shows the resulting fits and normalized RMSE for each of the four susceptibilities (each normalized by the difference between maximum and minimum of the respective ground truth susceptibilities). At an SNR = 50–100, all parameters were below 12% RMSE across all numbers of orientations. Computation time was around 10 min on an off-the-shelf laptop. Reasonable fitting accuracy was achieved for seven orientations and realistic frequency SNR. Furthermore, while decreasing the maximum tilt angle increased the RMSE, it did not completely erode the accuracy (still within 12% for SNR = 100 and maximum angle of 45°). Figures S7 and S8 show the resulting fits for varying tilt angle and sample orientations.

10991492, 2024, 8, Downloaded from https://analyticalsciencejournals.onlinelibrary.wiley.com/doi/10.1002/nbm.5150 by Cochrane Portugal, Wiley Online Library on [09/01/2025]. See the Terms and Conditions (https://onlinelibrary.wiley.com/terms-and-conditions) on Wiley Online Library for rules of use; OA articles are governed by the applicable Creative Commons License

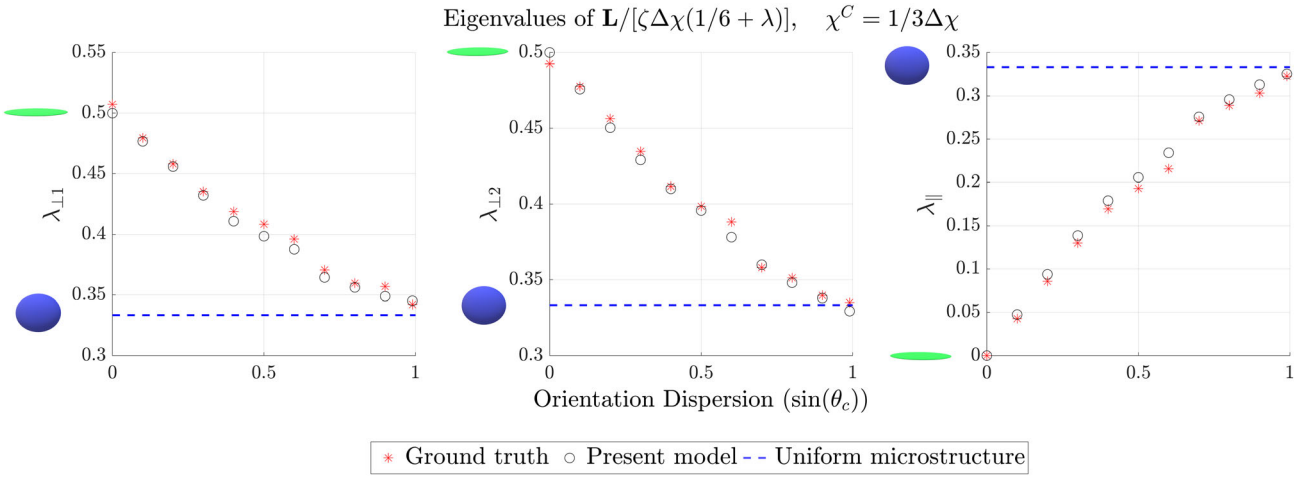

FIGURE 8 Simulation (a): simulation of the mesoscopic contribution from 11 different orientation distributions. Eigenvalues $(\lambda_{\perp 1}, \lambda_{\perp 1}\lambda_{\parallel})$ of ground truth $\mathbf{L}/[\zeta\Delta\chi(1+\lambda)/6]$ and model prediction $(\mathbf{I}-\mathbf{T})/2$ are presented for various levels of dispersion set by the maximum allowed polar angle $\sin(\theta_c)$, where $\chi^C = \Delta\chi/3$. Notice that the trace of $\mathbf{L}/[\zeta\Delta\chi(1+\lambda)/6]$ is 1. When $\sin(\theta_c) = 0$, $\overline{\Omega}^{\text{Meso}}$ is non-zero only perpendicular to the cylinder, as described by the green pancake. When $\sin(\theta_c) = 1$, $\overline{\Omega}^{\text{Meso}}$ is non-zero and isotropic, described by the blue sphere. Uniform microstructure defines the limit of uniform orientation dispersion.

5 | DISCUSSION

5.1 | Implications of biophysical model of WM on susceptibility estimation

Identifying the relevant biophysical parameters needed to characterize susceptibility-induced Larmor frequency shifts in MRI has been an active field of research for many years, and has led to many insightful biophysical models[11,13,14,34] of WM magnetic microstructure. However, despite this development, an ever-growing majority of QSM/STI experiments still effectively relies on the simplified description of tissue as a homogeneous liquid.[76] While such a model framework provides a simple analytical description and plausible looking images, it has the unfortunate downside of removing a potentially large specificity to magnetic microstructure, which inevitably biases susceptibility estimation,[23] and could prevent a deeper understanding of tissue's magnetic composition.[77]

Motivated by previous susceptibility models[9,11,13,14,24,34,36] and diffusion models,[5] which have included different features of microscopic structural anisotropy and microscopic susceptibility anisotropy, this study aimed to take another step towards a realistic description of magnetic microstructure. We modelled WM axons as a dense medium of long multi-layered cylinders with arbitrary orientation dispersion and microscopic susceptibility anisotropy originating from lipid chains forming the myelin sheaths. It further included spherical inclusions to model tissue iron and other similar contributors.

The mesoscopic contribution, Equation (27), depends in general on the scatter matrix $\mathbf{T}$, which can be written as a linear combination of $l = 2$ spherical harmonics Y_2^m. However, the functional behavior described by $a\sin^2\left(\theta_{\widehat{\mathbf{B}}}\right) + b$ in Equation (28), where $\theta_{\widehat{\mathbf{B}}}$ is the angle between the axons and magnetic field, has been observed in many experiments.[8,23,30,31] One may then be led to think that the fODF is axially symmetric, but typically these experiments only rotate the sample around a single fixed axis, which can give the impression of an axially symmetric fODF. Second, the fact that the frequency shift is non-zero at the magic angle has often been used as evidence of susceptibility anisotropy $\Delta\chi$, in accordance with the behavior for an axially symmetric fODF as seen in Figure 4A,B. However, as shown in Figure 5, a shift in the zero crossing can also be induced even for $\Delta\chi = 0$ when the fODF is not axially symmetric and the sample only rotated in a plane. This degeneracy becomes apparent when performing 3D rotations and can only be resolved by estimating orientation dispersion separately—for example, with dMRI, which in turn will reduce a potential bias in parameter estimation of susceptibility anisotropy when the fODF is not axially symmetric. As the fODF also affects the macroscopic contribution from neighboring voxels, the only contribution accounted for in STI,[22] we recommend estimating the fODF to obtain proper measurements of susceptibility anisotropy of WM axons.

Equation (25), describing the Lorentzian tensor $\mathbf{L}^S$ caused by the spherical magnetic susceptibility $\overline{\chi}^S$, shows the importance of considering a dense medium of magnetic microstructure. Here a substantial mesoscopic contribution $\overline{\Omega}^{\text{Meso}}$ from spheres is caused by a high density of cylinders reducing the available space for water molecules in an anisotropic way. This result may be particularly important when studying superficial WM,[42,43] which contains large amount of iron in the extra-axonal space.

Previous models[9,11,24,36] describing the mesoscopic frequency shift $\overline{\Omega}$ from WM axons relied on the ability to write the Lorentzian tensor as $\mathbf{L} = -\mathbf{N}\boldsymbol{\chi}$, i.e. as a product between a susceptibility tensor $\boldsymbol{\chi}$ and a purely structural tensor, here denoted as $\mathbf{N}$. However, as shown by Equation (3),

10991492, 2024, 8, Downloaded from https://analyticalsciencejournals.onlinelibrary.wiley.com/doi/10.1002/nbm.5150 by Cochrane Portugal, Wiley Online Library on [09/01/2025]. See the Terms and Conditions (https://onlinelibrary.wiley.com/terms-and-conditions) on Wiley Online Library for rules of use; OA articles are governed by the applicable Creative Commons License

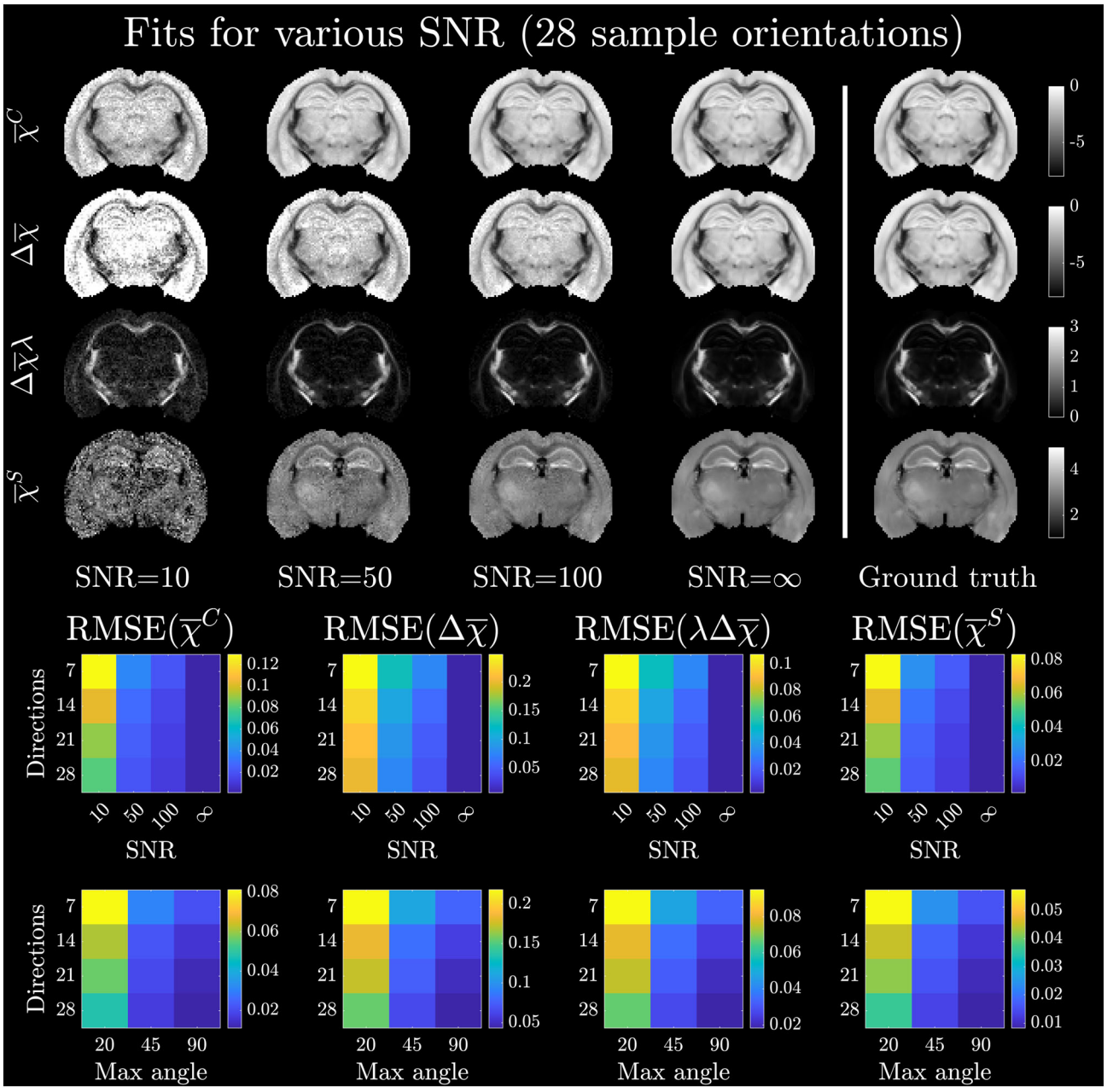

FIGURE 9 Simulation (b): susceptibility fitting maps. Fitting maps for various phase SNRs, and 28 directions. RMSE: RMSE for each parameter normalized by the range of susceptibility in each ground truth parameter. The first row shows variation in SNR, while the latter shows variation in tilt angle for a fixed SNR = 100.

L depends in general on the tensor-valued magneto-structural correlation function $\mathbf{\Gamma}(\boldsymbol{k})$. A relevant question is thus if and when **L** can be simplified to a product $\mathbf{N}\boldsymbol{\chi}$. Looking at the results in Equation (21), it is clear that the intra-axonal water, here appearing through λ, adds an additional frequency shift that cannot be derived from assuming a constant (scalar or tensor) magnetic susceptibility of the cylinders. This can be concluded from previous results showing that when the susceptibility of the cylinder is constant only structural correlations matter, and the mesoscopic frequency shifts in the intra- and extra-cylindrical compartments are the same.[24] If, however, the intra-cylindrical water is set to zero, such that the cylinders can be regarded as being solid, $\lambda = 0$ in Equation (21). In this case, the mesoscopic frequency shift generated by every single solid cylinder can in fact be described by a product of the form $\mathbf{N}(\widehat{\boldsymbol{n}})\overline{\chi}(\widehat{\boldsymbol{n}})$, where $\overline{\chi}(\widehat{\boldsymbol{n}}) = \overline{\chi}^C\mathbf{I} - \Delta\overline{\chi}\left(\widehat{\boldsymbol{n}}\widehat{\boldsymbol{n}}^{\mathsf{T}} - \mathbf{I}/3\right)/2$ is the mean magnetic susceptibility (cf. Equation (19)) and $\mathbf{N}(\widehat{\boldsymbol{n}}) = \left(\widehat{\boldsymbol{n}}\widehat{\boldsymbol{n}}^{\mathsf{T}} - \mathbf{I}/3\right)/2$ the demagnetization tensor[9] for a cylinder pointing along $\widehat{\boldsymbol{n}}$. However, upon summing over multiple cylinders with different orientations, it is in general not possible to write **L** as a product. The only exception to this statement is when axons are oriented axially symmetrically around some $\widehat{\boldsymbol{n}}$, in which case **L** is a product of the form $p_2\mathbf{N}(\widehat{\boldsymbol{n}})\overline{\chi}(\widehat{\boldsymbol{n}})$.

10991492, 2024, 8, Downloaded from https://analyticalsciencejournals.onlinelibrary.wiley.com/doi/10.1002/nbm.5150 by Cochrane Portugal, Wiley Online Library on [09/01/2025]. See the Terms and Conditions (https://onlinelibrary.wiley.com/terms-and-conditions) on Wiley Online Library for rules of use; OA articles are governed by the applicable Creative Commons License

5.1.1 | Limitations and future model extensions

The proposed WM model is valid when the signal is adequately described by the first signal cumulant $\overline{\Omega}_{\mathrm{MRI}}t$, which is the case in the DNR (see the discussion in our previous study[9]). While the first cumulant is also sufficient in the weak static dephasing regime, the measured signal $S(t)$ would likely depend on MW frequency shifts and other fast relaxing water pools, which are still not fully understood.[28,78] MW may also affect the frequency shift through exchange with the surrounding water. The approximation of the signal in terms of the first cumulant can be violated for different reasons. It is violated in regions with high levels of iron or calcium, where the signal averaging is not equivalent to phase averaging.[40] Clustering of iron in neuroglia or within the axonal water compartments may also be of importance, but is so far less understood compared with GM.[79,80] We therefore plan to investigate WM iron in the future and extend our model to account for any additional frequency effects. Second, it is well known that water is compartmentalized in WM, which can be seen from dMRI experiments.[81,82] Hence in DNR, the tissue is expected to have many intra-axonal compartments and extra-axonal compartments—even in fixated tissue. Luckily, when the phase is small, which is a main assumption in this study, one can perform a cumulant expansion of the compartmentalized signal, which yields $S(t) = \exp\left(-i\overline{\Omega}_{\mathrm{MRI}}t - R_2 t + \mathcal{O}\left(\delta\Omega^2 t^2\right)\right)$. Here, the exponent becomes a power series in $\delta\Omega t$ corresponding to the typical phase shift and the linear term is the first cumulant $\overline{\Omega}_{\mathrm{MRI}}$ of the whole signal (cf. Equation (1)). Nevertheless, analyzing the individual compartments' signals could be used to gain a deeper insight into the mesoscopic frequency shifts from different susceptibility sources, including their relaxation rates and water fractions,[13,57,59,60,83] which can change the sensitivity to different susceptibility sources in different compartments: for example, extra-axonal iron will affect intra-axonal water differently from extra-axonal water and so on. This will be pursued in depth in future studies. Diffusion filtering can be used to change the relative weights of water compartments in the signal. For such techniques, our model framework can be used to describe frequency shifts from specific water compartments, e.g. intra-axonal water.[84] Incorporating the susceptibility model into diffusion models will be considered in future studies.[85–89] Recent susceptibility models[90] combine fitting of relaxation rates and frequency shifts to disentangle para- and diamagnetic sources in brain tissue. However, such models have so far disregarded mesoscopic frequency contributions, similarly to QSM. Nevertheless, the contrast from the estimated sources has shown great promise when compared with histology. It would therefore be of interest to expand the analytical framework presented here to derive an analytical solution for transverse relaxation.

While the analytical results have been validated numerically, the model remains to be validated against real WM tissue where axons exhibit beading, undulations, non-circular cross-sections, etc.[26,62,91] Scrutinizing the model with realistic in silico substrates acquired with 3D electron microscopy[26] will therefore be considered in future studies.

5.2 | Feasibility of solving inverse problem

Simulation (b) investigated the solution to the inverse problem in a digital brain phantom. The positive results suggest that successful model estimation in humans in vivo, where maximum tilt angle and number of orientations are limiting factors, is feasible. The reason why susceptibility parameters can be estimated despite small tilt angles is that the tensor structure is already determined from diffusion. This leaves only four orientationally invariant susceptibility parameters to be determined in each voxel, if the mesoscopic frequency shift from spheres (cf. Equation (25)) can be neglected. While this assumption could be violated in real WM, additional information about the axonal volume fraction may be needed to successfully solve the inverse problem. Alternatively, the mesoscopic frequency shift could be included in the inverse problem as $\overline{\Omega}^{\mathrm{Meso}}\left(\widehat{\mathbf{B}}\right) = a\widehat{\mathbf{B}}^{\mathrm{T}}\mathbf{T}\widehat{\mathbf{B}} + b$, analogous to Equation (28), but at the expense of being unable to separate $\overline{\chi}^{C}$ and $\overline{\chi}^{S}$. Qualitatively, the maps in Figure 9 still appear slightly noisy, especially $\overline{\chi}^{S}$ in GM. This makes sense, as $\overline{\chi}^{S}$ in the phantom only has a macroscopic contribution $\overline{\Omega}^{\mathrm{Macro}}_{\chi^S}\left(\widehat{\mathbf{B}}\right)$ to the Larmor frequency $\overline{\Omega}_{\mathrm{MRI}}\left(\widehat{\mathbf{B}}\right)$, and is difficult to disentangle from $\overline{\chi}^{C}$ when $\overline{\Omega}^{\mathrm{Meso}}_{\chi^C}\left(\widehat{\mathbf{B}}\right)$ is close to zero (the two sources give rise to similar macroscopic frequency shifts). Weighted least squares or regularization may further help to decrease such degeneracy and reduce RMSE. Other limiting factors that may affect the fitting performance are noise in the fODF estimation, background field removal and unwrapping of the frequency shift,[92] and finding an optimal stopping criterion (e.g., L-curve optimization[93–95]) for the fitting routine when no ground truth is available. All such potential confounding factors will be explored in future studies. In simulation (b), mesoscopic contributions from the spheres were disregarded. If this contribution is too large to ignore, it can make the inverse problem harder to solve. This is because the mesoscopic contribution from spheres is scaled by the cylinder volume fraction ζ^{C}, in contrast to the macroscopic contribution, Equation (22), which adds an additional degree of freedom to the inverse problem.

5.3 | Wharton and Bowtell residual frequency shift f_R

Because of the comprehensive theoretical framework involved, we dedicated this work to a detailed presentation and analysis of the WM biophysical model for the Larmor frequency shift, leaving experimental validation as a future endeavor. However, an insightful study has already been performed by Wharton and Bowtell[23] in the spirit of previous experiments by Luo et al.[8] and Lee et al.[33] In their study, a fresh porcine

10991492, 2024, 8, Downloaded from https://analyticalsciencejournals.onlinelibrary.wiley.com/doi/10.1002/nbm.5150 by Cochrane Portugal, Wiley Online Library on [09/01/2025]. See the Terms and Conditions (https://onlinelibrary.wiley.com/terms-and-conditions) on Wiley Online Library for rules of use; OA articles are governed by the applicable Creative Commons License

optical nerve was cast in agarose gel in a spherical container and scanned at multiple sample orientations to the scanner field. By measuring the frequency external to the optical nerve, it was possible to determine an average macroscopic frequency shift $\overline{\Omega}^{\text{Macro}}$ in a cylindrical shell surrounding the nerve. This was achieved with computer simulations by digitizing a sample mask in place of the sample, and then finding the optimal WM bulk susceptibility values $(\overline{\chi}^C, \Delta\overline{\chi}) = (\chi_I, \frac{3}{2}\chi_A)$ to describe the average frequency outside. In this way, the authors found $\chi_I = -0.082$ ppm and χ_A 0.011 ppm. Next, they estimated a residual frequency shift $f_R = a\sin^2\left(\theta_{\widehat{\mathbf{B}}}\right) + b$ with $a = -5.59$ Hz and $b = 4.88$ Hz, which defined the remaining frequency shift inside the sample in addition to the one that could be explained by the bulk susceptibilities $(\overline{\chi}^C, \Delta\overline{\chi})$. Based on the model proposed herein, f_R should directly correspond to the sample averaged mesoscopic frequency contribution $\overline{\Omega}^{\text{Meso}}$, assuming that chemical exchange and other frequency inducing effects can be neglected. By plugging the previously mentioned susceptibility values into our WM model, Equation (28), assuming an axially symmetric fODF, we can attempt to predict the values of a and b describing f_R. Making the naive assumption that no water resides in bilayers or intra-axonal space ($\lambda = 0$), and that axons are parallel ($p_2 = 1$), $a' = -12.6$ Hz and $b' = 8.7$ Hz. Both are around a factor of 2 higher than reported by Wharton and Bowtell. This is not unexpected since orientation dispersion has not been accounted for so far, and since the mesoscopic contribution depends differently on magnetic susceptibility of spherical inclusions, in comparison with the macroscopic contribution. To obtain a rough idea of the size of such corrections, we assume that the orientation dispersion can be described by a Watson fODF. Assuming that porcine optic nerve dispersion is similar to WM in the spinal cord, that is, around 20°,[68] this would approximately result in $p_2 = 0.8$. Based on human WM,[69] we estimate $\lambda \sim 1.6$ with the net result that $a' = -9.4$ Hz and $b' = 7.2$ Hz. While this is closer to the measured residual frequency, the estimate still does not agree completely with the experiment. The remaining discrepancy could however be attributed to a negative difference between the susceptibility of the agarose and the fluid inside the nerve. For example, if fluid inside the nerve is slightly more diamagnetic, the fitted χ_I overestimates the WM susceptibility. If so, the coefficients decrease and come into agreement with f_R. While the latter correction is somewhat far-fetched, it nevertheless demonstrates that, by including dispersion, intra-axonal water and a slightly more diamagnetic tissue fluid compared with agarose, the WM model offers an interpretation of the measured residual frequency. This would however require additional experiments to be established. Another potential reason for the discrepancy could originate from MW, which has been found to exhibit large frequency shifts that go beyond the presented WM model.[11,13,28,59,78] Since the experiment by Wharton and Bowtell used a 7 T scanner with echo times comparable to T_2^* of MW,[57,59] f_R would also reflect the frequency shift from within the MW. A future aim is therefore to repeat the experiment and include measurements of orientation dispersion with dMRI, acquire multiple echo times to investigate the time dependence of the Larmor frequency, examine the effect from agarose chemical shifts and perhaps improve upon the susceptibility matching to eliminate potential non-microstructural corrections. This may lead to a better understanding of how well f_R can be described by the modelled effects of WM magnetic microstructure and what goes beyond.

6 | CONCLUSION

We have presented an analytical expression for the measured Larmor frequency shift from a biophysical model of WM magnetic microstructure. The model is arguably the most realistic biophysical model for the frequency shift in WM to date, and includes axons with microscopic WM susceptibility anisotropy, intra-compartmental water, and spherical inclusions with scalar susceptibility such as biologically stored iron. Our analytical results for the measured Larmor frequency shift are described in terms of rotation-invariant susceptibility parameters. The structural orientation dependence of axons is described in terms of a fiber orientation distribution, which must be determined independently using, for example, dMRI. We validated our analytical results with numerical simulations and demonstrated the feasibility of inverting our model to estimate underlying rotation-invariant susceptibility parameters on a digital brain phantom.

ACKNOWLEDGMENTS

This study is funded by the Independent Research Fund (grants 8020-00158B and 3103-00144B) and Lundbeck BrainComet (grant R310-2018-3455). Fitting codes are available on request.

CONFLICT OF INTEREST STATEMENT

The authors declare no conflict of interest.

ORCID

Anders Dyhr Sandgaard https://orcid.org/0000-0001-8728-375X
Noam Shemesh https://orcid.org/0000-0001-6681-5876
Leif Østergaard https://orcid.org/0000-0003-2930-6997
Valerij G. Kiselev https://orcid.org/0000-0002-5349-5399
Sune Nørhøj Jespersen https://orcid.org/0000-0003-3146-4329

10991492, 2024, 8, Downloaded from https://analyticalsciencejournals.onlinelibrary.wiley.com/doi/10.1002/nbm.5150 by Cochrane Portugal, Wiley Online Library on [09/01/2025]. See the Terms and Conditions (https://onlinelibrary.wiley.com/terms-and-conditions) on Wiley Online Library for rules of use; OA articles are governed by the applicable Creative Commons License

REFERENCES

1. Love S. Demyelinating diseases. *J Clin Pathol*. 2006;59(11):1151-1159. doi:10.1136/jcp.2005.031195
2. Grech R, Grech S, Mizzi A. Intracranial calcifications: a pictorial review. *Neuroradiol J*. 2012;25(4):427-451. doi:10.1177/197140091202500406
3. Ndayisaba A, Kaindlstorfer C, Wenning GK. Iron in neurodegeneration—cause or consequence? *Front Neurosci*. 2019;13:180. doi:10.3389/fnins.2019.00180
4. Eskreis-Winkler S, Zhang Y, et al. The clinical utility of QSM: disease diagnosis, medical management, and surgical planning. *NMR Biomed*. 2017;30(4):e3668. doi:10.1002/nbm.3668
5. Novikov DS, Fieremans E, Jespersen SN, Kiselev VG. Quantifying brain microstructure with diffusion MRI: theory and parameter estimation. *NMR Biomed*. 2019;32(4):e3998. doi:10.1002/NBM.3998
6. Ruh A, Scherer H, Kiselev VG. The Larmor frequency shift in magnetically heterogeneous media depends on their mesoscopic structure. *Magn Reson Med*. 2018;79(2):1101-1110. doi:10.1002/mrm.26753
7. Durrant CJ, Hertzberg MP, Kuchel PW. Magnetic susceptibility: further insights into macroscopic and microscopic fields and the sphere of Lorentz. *Concepts Magn Reson A*. 2003;18A(1):72-95. doi:10.1002/CMR.A.10067
8. Luo J, He X, Yablonskiy DA. Magnetic susceptibility induced white matter MR signal frequency shifts—experimental comparison between Lorentzian sphere and generalized Lorentzian approaches. *Magn Reson Med*. 2014;71(3):1251-1263. doi:10.1002/MRM.24762
9. Sandgaard AD, Shemesh N, Kiselev VG, Jespersen SN. Larmor frequency shift from magnetized cylinders with arbitrary orientation distribution. *NMR Biomed*. 2023;36(3):e4859. doi:10.1002/nbm.4859
10. Haacke EM, Xu Y, Cheng YCN, Reichenbach JR. Susceptibility weighted imaging (SWI). *Magn Reson Med*. 2004;52(3):612-618. doi:10.1002/mrm.20198
11. Yablonskiy DA, Sukstanskii AL. Generalized Lorentzian Tensor Approach (GLTA) as a biophysical background for quantitative susceptibility mapping. *Magn Reson Med*. 2015;73(2):757-764. doi:10.1002/mrm.25538
12. Chu K-C, Xu Y, Balschi JA, Springer CS Jr. Bulk magnetic susceptibility shifts in NMR studies of compartmentalized samples: use of paramagnetic reagents. *Magn Reson Med*. 1990;13(2):239-262. doi:10.1002/MRM.1910130207
13. Wharton S, Bowtell R. Fiber orientation-dependent white matter contrast in gradient echo MRI. *Proc Natl Acad Sci U S A*. 2012;109(45):18559-18564. doi:10.1073/pnas.1211075109
14. Sukstanskii AL, Yablonskiy DA. On the role of neuronal magnetic susceptibility and structure symmetry on gradient echo MR signal formation. *Magn Reson Med*. 2014;71(1):345-353. doi:10.1002/mrm.24629
15. Marques JP, Bowtell R. Application of a Fourier-based method for rapid calculation of field inhomogeneity due to spatial variation of magnetic susceptibility. *Concepts Magn Reson B*. 2005;25B(1):65-78. doi:10.1002/cmr.b.20034
16. Salomir R, de Senneville BD, Moonen CT. A fast calculation method for magnetic field inhomogeneity due to an arbitrary distribution of bulk susceptibility. *Concepts Magn Reson*. 2003;19B(1):26-34. doi:10.1002/cmr.b.10083
17. Jenkinson M, Wilson JL, Jezzard P. Perturbation method for magnetic field calculations of nonconductive objects. *Magn Reson Med*. 2004;52(3):471-477. doi:10.1002/mrm.20194
18. Newell AJ, Williams W, Dunlop DJ. A generalization of the demagnetizing tensor for nonuniform magnetization. *J Geophys Res*. 1993;98(B6):9551-9555. doi:10.1029/93JB00694
19. Aharoni A. Demagnetizing factors for rectangular ferromagnetic prisms. *J Appl Phys*. 1998;83(6):3432-3434. doi:10.1063/1.367113
20. Dickinson WC. The time average magnetic field at the nucleus in nuclear magnetic resonance experiments. *Phys Rev*. 1951;81(5):717-731. doi:10.1103/PhysRev.81.717
21. Deistung A, Schweser F, Reichenbach JR. Overview of quantitative susceptibility mapping. *NMR Biomed*. 2017;30(4):e3569. doi:10.1002/nbm.3569
22. Liu C. Susceptibility tensor imaging. *Magn Reson Med*. 2010;63(6):1471-1477. doi:10.1002/mrm.22482
23. Wharton S, Bowtell R. Effects of white matter microstructure on phase and susceptibility maps. *Magn Reson Med*. 2015;73(3):1258-1269. doi:10.1002/mrm.25189
24. Sandgaard AD, Kiselev VG, Henriques RN, Shemesh N, Jespersen SN. Incorporating the effect of white matter microstructure in the estimation of magnetic susceptibility in ex vivo mouse brain. *Magn Reson Med*. 2024;91(2):699-715. doi:10.1002/MRM.29867
25. Lounila J, Ala-Korpela M, Jokisaari J, Savolainen MJ, Kesäniemi YA. Effects of orientational order and particle size on the NMR line positions of lipoproteins. *Phys Rev Lett*. 1994;72(25):4049-4052. doi:10.1103/PhysRevLett.72.4049
26. Abdollahzadeh A, Belevich I, Jokitalo E, Sierra A, Tohka J. DeepACSON automated segmentation of white matter in 3D electron microscopy. *Commun Biol*. 2021;4(1):179. doi:10.1038/s42003-021-01699-w
27. Mount CW, Monje M. Wrapped to adapt: experience-dependent myelination. *Neuron*. 2017;95(4):743-756. doi:10.1016/J.NEURON.2017.07.009
28. Duyn JH. Frequency shifts in the myelin water compartment. *Magn Reson Med*. 2014;71(6):1953-1955. doi:10.1002/mrm.24983
29. Min Y, Kristiansen K, Boggs JM, Husted C, Zasadzinski JA, Israelachvili J. Interaction forces and adhesion of supported myelin lipid bilayers modulated by myelin basic protein. *Proc Natl Acad Sci U S A*. 2009;106(9):3154-3159. doi:10.1073/pnas.0813110106
30. Rudko DA, Klassen LM, De Chickera SN, Gati JS, Dekaban GA, Menon RS. Origins of R2* orientation dependence in gray and white matter. *Proc Natl Acad Sci U S A*. 2014;111(1):E159-E167. doi:10.1073/PNAS.1306516111
31. Denk C, Torres EH, Mackay A, Rauscher A. The influence of white matter fibre orientation on MR signal phase and decay. *NMR Biomed*. 2011;24(3):246-252. doi:10.1002/NBM.1581
32. Van Gelderen P, Mandelkow H, De Zwart JA, Duyn JH. A torque balance measurement of anisotropy of the magnetic susceptibility in white matter. *Magn Reson Med*. 2015;74(5):1388-1396. doi:10.1002/mrm.25524
33. Lee J, Shmueli K, Fukunaga M, et al. Sensitivity of MRI resonance frequency to the orientation of brain tissue microstructure. *Proc Natl Acad Sci U S A*. 2010;107(11):5130-5135. doi:10.1073/pnas.0910222107
34. He X, Yablonskiy DA. Biophysical mechanisms of phase contrast in gradient echo MRI. *Proc Natl Acad Sci U S A*. 2009;106(32):13558-13563. doi:10.1073/pnas.0904899106
35. Ruh A, Emerich P, Scherer H, Novikov DS, Kiselev VG. Observation of magnetic structural universality and jamming transition with NMR. *J Magn Reson*. 2023;353:107476. doi:10.1016/J.JMR.2023.107476
36. Kiselev VG. Larmor frequency in heterogeneous media. *J Magn Reson*. 2019;299:168-175. doi:10.1016/j.jmr.2018.12.008

10991492, 2024, 8, Downloaded from https://analyticalsciencejournals.onlinelibrary.wiley.com/doi/10.1002/nbm.5150 by Cochrane Portugal, Wiley Online Library on [09/01/2025]. See the Terms and Conditions (https://onlinelibrary.wiley.com/terms-and-conditions) on Wiley Online Library for rules of use; OA articles are governed by the applicable Creative Commons License

37. Lorentz HA. Uber die Beziehung zwischen der Fortpflanzungsgeschwindigkeit des Lichtes und der Korperdichte. *Ann Phys*. 1880;245:641-665.
38. Lorentz HA. *The theory of electrons*, 2nd ed. Leipzig, Germany: B.G. Teubner; 1916.
39. Ruh A, Kiselev VG. Calculation of Larmor precession frequency in magnetically heterogeneous media. *Concepts Magn Reson A*. 2018;47A(1):e21472. doi:10.1002/cmr.a.21472
40. Yablonskiy DA, Haacke EM. Theory of NMR signal behavior in magnetically inhomogeneous tissues: the static dephasing regime. *Magn Reson Med*. 1994;32(6):749-763. doi:10.1002/mrm.1910320610
41. Ronen I, Budde M, Ercan E, Annese J, Techawiboonwong A, Webb A. Microstructural organization of axons in the human corpus callosum quantified by diffusion-weighted magnetic resonance spectroscopy of N-acetylaspartate and post-mortem histology. *Brain Struct Funct*. 2014;219(5):1773-1785. doi:10.1007/s00429-013-0600-0
42. Fukunaga M, Li TQ, Van Gelderen P, et al. Layer-specific variation of iron content in cerebral cortex as a source of MRI contrast. *Proc Natl Acad Sci U S A*. 2010;107(8):3834-3839. doi:10.1073/pnas.0911177107
43. Kirilina E, Helbling S, Morawski M, et al. Superficial white matter imaging: contrast mechanisms and whole-brain in vivo mapping. *Sci Adv*. 2020;6(41): eaaz9281. doi:10.1126/SCIADV.AAZ9281/SUPPL_FILE/AAZ9281_SM.PDF
44. Marques JP, Maddage R, Mlynarik V, Gruetter R. On the origin of the MR image phase contrast: an in vivo MR microscopy study of the rat brain at 14.1 T. *NeuroImage*. 2009;46(2):345-352. doi:10.1016/J.NEUROIMAGE.2009.02.023
45. Liu C, Li W, Johnson GA, Wu B. High-field (9.4 T) MRI of brain dysmyelination by quantitative mapping of magnetic susceptibility. *NeuroImage*. 2011; 56(3):930-938. doi:10.1016/J.NEUROIMAGE.2011.02.024
46. Lee J, Shmueli K, Kang BT, et al. The contribution of myelin to magnetic susceptibility-weighted contrasts in high-field MRI of the brain. *NeuroImage*. 2012;59(4):3967-3975. doi:10.1016/J.NEUROIMAGE.2011.10.076
47. Kiselev VG. Fundamentals of diffusion MRI physics. *NMR Biomed*. 2017;30(3):e3602. doi:10.1002/nbm.3602
48. Osborn JA. Demagnetizing factors of the general ellipsoid. *Phys Rev*. 1945;67(11/12):351-357. doi:10.1103/PhysRev.67.351
49. Moskowitz R, Della TE. Theoretical aspects of demagnetization tensors. *IEEE Trans Magn*. 1966;2(4):739-744. doi:10.1109/TMAG.1966.1065973
50. van der Knaap MS, Valk J. Myelin and white matter. In: *Magnetic Resonance of Myelination and Myelin Disorders*. Springer; 2005:1-19. doi:10.1007/3-540-27660-2_1
51. Cheng JX, Pautot S, Weitz DA, Xie XS. Ordering of water molecules between phospholipid bilayers visualized by coherent anti-Stokes Raman scattering microscopy. *Proc Natl Acad Sci U S A*. 2003;100(17):9826-9830. doi:10.1073/pnas.1732202100
52. Connor JR, Menzies SL. Relationship of iron to oligodendrocytes and myelination. *Glia*. 1996;17(2):83-93. doi:10.1002/(SICI)1098-1136(199606)17:2
53. Duyn JH, Schenck J. Contributions to magnetic susceptibility of brain tissue. *NMR Biomed*. 2017;30(4):e3546. doi:10.1002/nbm.3546
54. Rutledge JN, Hilal SK, Silver AJ, Defendini R, Fahn S. Study of movement disorders and brain iron by MR. *Am J Roentgenol*. 1987;149(2):365-379. doi:10.2214/AJR.149.2.365
55. Ruh A, Kiselev VG. Larmor frequency dependence on structural anisotropy of magnetically heterogeneous media. *J Magn Reson*. 2019;307:106584. doi:10.1016/j.jmr.2019.106584
56. van der Knaap MS, Valk J. *Magnetic Resonance of Myelination and Myelin Disorders*. Springer; 2005. doi:10.1007/3-540-27660-2
57. Nam Y, Lee J, Hwang D, Kim DH. Improved estimation of myelin water fraction using complex model fitting. *NeuroImage*. 2015;116:214-221. doi:10.1016/J.NEUROIMAGE.2015.03.081
58. Hédouin R, Metere R, Chan KS, et al. Decoding the microstructural properties of white matter using realistic models. *NeuroImage*. 2021;237:118138. doi:10.1016/j.neuroimage.2021.118138
59. Sati P, van Gelderen P, Silva AC, et al. Micro-compartment specific T2* relaxation in the brain. *NeuroImage*. 2013;77:268-278. doi:10.1016/J.NEUROIMAGE.2013.03.005
60. Van Gelderen P, De Zwart JA, Lee J, Sati P, Reich DS, Duyn JH. Nonexponential T2* decay in white matter. *Magn Reson Med*. 2012;67(1):110-117. doi:10.1002/mrm.22990
61. Fisher NI, Lewis T, Embleton BJJ. *Statistical Analysis of Spherical Data*. Cambridge University Press; 1987. doi:10.1017/CBO9780511623059
62. Lee H-HH, Yaros K, Veraart J, et al. Along-axon diameter variation and axonal orientation dispersion revealed with 3D electron microscopy: implications for quantifying brain white matter microstructure with histology and diffusion MRI. *Brain Struct Funct*. 2019;224(4):1469-1488. doi:10.1007/s00429-019-01844-6
63. Thorne KS. Multipole expansions of gravitational radiation. *Rev Mod Phys*. 1980;52(2):299-339. doi:10.1103/RevModPhys.52.299
64. Liu C, Li W, Wu B, Jiang Y, Johnson GA. 3D fiber tractography with susceptibility tensor imaging. *NeuroImage*. 2012;59(2):1290-1298. doi:10.1016/J.NEUROIMAGE.2011.07.096
65. Novikov DS, Veraart J, Jelescu IO, Fieremans E. Rotationally-invariant mapping of scalar and orientational metrics of neuronal microstructure with diffusion MRI. *NeuroImage*. 2018;174:518-538. doi:10.1016/J.NEUROIMAGE.2018.03.006
66. Reisert M, Kellner E, Dhital B, Hennig J, Kiselev VG. Disentangling micro from mesostructure by diffusion MRI: a Bayesian approach. *NeuroImage*. 2017;147:964-975. doi:10.1016/J.NEUROIMAGE.2016.09.058
67. Bingham C. An antipodally symmetric distribution on the sphere. *Ann Stat*. 2007;2(6):1201-1225. doi:10.1214/aos/1176342874
68. Jespersen SN, Olesen JL, Hansen B, Shemesh N. Diffusion time dependence of microstructural parameters in fixed spinal cord. *NeuroImage*. 2018;182: 329-342. doi:10.1016/J.NEUROIMAGE.2017.08.039
69. Aboitiz F, Scheibel AB, Fisher RS, Zaidel E. Fiber composition of the human corpus callosum. *Brain Res*. 1992;598(1/2):143-153. doi:10.1016/0006-8993(92)90178-C
70. Sandgaard AD, Shemesh N, Jespersen SN, Kiselev VG. To mask or not to mask? Investigating the impact of accounting for spatial frequency distributions and susceptibility sources on QSM quality. *Magn Reson Med*. 2023;90(1):353-362. doi:10.1002/MRM.29627
71. Fong DCL, Saunders M. LSMR: an iterative algorithm for sparse least-squares problems. *SIAM J Sci Comput*. 2011;33:2950-2971. doi:10.1137/10079687X
72. Penny W, Friston K, Ashburner J, Kiebel S, Nichols T. *Statistical Parametric Mapping: The Analysis of Functional Brain Images*. Academic Press; 2007. doi:10.1016/B978-0-12-372560-8.X5000-1
73. Jensen JH, Helpern JA, Ramani A, Lu H, Kaczynski K. Diffusional kurtosis imaging: the quantification of non-Gaussian water diffusion by means of magnetic resonance imaging. *Magn Reson Med*. 2005;53(6):1432-1440. doi:10.1002/mrm.20508

10991492, 2024, 8, Downloaded from https://analyticalsciencejournals.onlinelibrary.wiley.com/doi/10.1002/nbm.5150 by Cochrane Portugal, Wiley Online Library on [09/01/2025]. See the Terms and Conditions (https://onlinelibrary.wiley.com/terms-and-conditions) on Wiley Online Library for rules of use; OA articles are governed by the applicable Creative Commons License

74. Jensen JH, Russell Glenn G, Helpern JA. Fiber ball imaging. *NeuroImage*. 2016;124(A):824-833. doi:10.1016/j.neuroimage.2015.09.049
75. Jones DK, Horsfield MA, Simmons A. Optimal strategies for measuring diffusion in anisotropic systems by magnetic resonance imaging. *Magn Reson Med*. 1999;42(3):515-525. doi:10.1002/(SICI)1522-2594(199909)42:33.0.CO;2-Q
76. Schäfer A, Wharton S, Gowland P, Bowtell R. Using magnetic field simulation to study susceptibility-related phase contrast in gradient echo MRI. *NeuroImage*. 2009;48(1):126-137. doi:10.1016/J.NEUROIMAGE.2009.05.093
77. Novikov DS, Kiselev VG, Jespersen SN. On modeling. *Magn Reson Med*. 2018;79(6):3172-3193. doi:10.1002/MRM.27101
78. Yablonskiy DA, Sukstanskii AL. Biophysical mechanisms of myelin-induced water frequency shifts. *Magn Reson Med*. 2014;71(6):1956-1958. doi:10.1002/mrm.25214
79. Wen J, Goyal MS, Astafiev SV, Raichle ME, Yablonskiy DA. Genetically defined cellular correlates of the baseline brain MRI signal. *Proc Natl Acad Sci U S A*. 2018;115(41):E9727-E9736. doi:10.1073/PNAS.1808121115/SUPPL_FILE/PNAS.1808121115.SD08.XLS
80. Brammerloh M, Morawski M, Friedrich I, et al. Measuring the iron content of dopaminergic neurons in substantia nigra with MRI relaxometry. *NeuroImage*. 2021;239:118255. doi:10.1016/J.NEUROIMAGE.2021.118255
81. Veraart J, Nunes D, Rudrapatna U, et al. Noninvasive quantification of axon radii using diffusion MRI. *eLife*. 2020;9:9. doi:10.7554/ELIFE.49855
82. Olesen JL, Østergaard L, Shemesh N, Jespersen SN. Diffusion time dependence, power-law scaling, and exchange in gray matter. *NeuroImage*. 2022;251:118976. doi:10.1016/J.NEUROIMAGE.2022.118976
83. Wharton S, Bowtell R. Gradient echo based fiber orientation mapping using R2* and frequency difference measurements. *NeuroImage*. 2013;83:1011-1023. doi:10.1016/J.NEUROIMAGE.2013.07.054
84. Cottaar M, Wu W, Tendler BC, Nagy Z, Miller K, Jbabdi S. Quantifying myelin in crossing fibers using diffusion-prepared phase imaging: theory and simulations. *Magn Reson Med*. 2021;86(5):2618-2634. doi:10.1002/MRM.28907
85. Sandgaard AD, Kiselev VG, Shemesh N, Jespersen SN. Incorporating susceptibility effects into the standard model of diffusion in white matter. Paper presented at: ISMRM & ISMRT Annual Meeting & Exhibition; June 3-8, 2023:0975; Toronto, ON, Canada. https://www.ismrm.org/23/program-files/PP-11.htm
86. Kleban E, Tax CMW, Rudrapatna US, Jones DK, Bowtell R. Strong diffusion gradients allow the separation of intra- and extra-axonal gradient-echo signals in the human brain. *NeuroImage*. 2020;217:116793. doi:10.1016/J.NEUROIMAGE.2020.116793
87. Tax CMW, Kleban E, Chamberland M, Baraković M, Rudrapatna U, Jones DK. Measuring compartmental T2-orientational dependence in human brain white matter using a tiltable RF coil and diffusion-T2 correlation MRI. *NeuroImage*. 2021;236:117967. doi:10.1016/J.NEUROIMAGE.2021.117967
88. Dell'Acqua VP, Tax CMW, Molendowska M, Jones DK, Kleban E, Parker GD. Measuring compartmental T2 and T2* orientation dependence in white matter. Paper presented at: ISMRM Workshop on Diffusion MRI: from Research to Clinic; ISMRM. October 10-14, 2022; Amsterdam, The Netherlands.
89. Álvarez GA, Shemesh N, Frydman L. Internal gradient distributions: a susceptibility-derived tensor delivering morphologies by magnetic resonance. *Sci Rep*. 2017;7(1):3311. doi:10.1038/s41598-017-03277-9
90. Shin H-G, Lee J, Yun YH, et al. χ-separation: magnetic susceptibility source separation toward iron and myelin mapping in the brain. *NeuroImage*. 2021;240:118371. doi:10.1016/J.NEUROIMAGE.2021.118371
91. Andersson M, Kjer HM, Rafael-Patino J, et al. Axon morphology is modulated by the local environment and impacts the noninvasive investigation of its structure–function relationship. *Proc Natl Acad Sci U S A*. 2021;117(52):33649-33659. doi:10.1073/PNAS.2012533117
92. Marques JP, Meineke J, Milovic C, et al. QSM reconstruction challenge 2.0: a realistic in silico head phantom for MRI data simulation and evaluation of susceptibility mapping procedures. *Magn Reson Med*. 2021;86(1):526-542. doi:10.1002/MRM.28716
93. Hansen PC, Jensen TK, Rodriguez G. An adaptive pruning algorithm for the discrete L-curve criterion. *J Comput Appl Math*. 2007;198(2):483-492. doi:10.1016/J.CAM.2005.09.026
94. Hansen PC, O'Leary DP. The use of the L-curve in the regularization of discrete ill-posed problems. *SIAM J Sci Comput*. 1993;14(6):1487-1503. doi:10.1137/0914086
95. Hansen PC. The L-curve and its use in the numerical treatment of inverse problems. In: Johnston P, ed. *Computational Inverse Problems in Electrocardiology*. Advances in Computational Bioengineering. Vol.4. WIT Press; 2000:119-142.

SUPPORTING INFORMATION

Additional supporting information can be found online in the Supporting Information section at the end of this article.

How to cite this article: Sandgaard AD, Shemesh N, Østergaard L, Kiselev VG, Jespersen SN. The Larmor frequency shift of a white matter magnetic microstructure model with multiple sources. *NMR in Biomedicine*. 2024;37(8):e5150. doi:10.1002/nbm.5150

10991492, 2024, 8, Downloaded from https://analyticalsciencejournals.onlinelibrary.wiley.com/doi/10.1002/nbm.5150 by Cochrane Portugal, Wiley Online Library on [09/01/2025]. See the Terms and Conditions (https://onlinelibrary.wiley.com/terms-and-conditions) on Wiley Online Library for rules of use; OA articles are governed by the applicable Creative Commons License